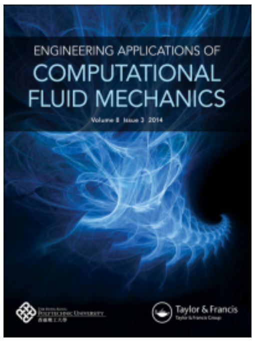

Taylor & Francis
Taylor & Francis Group

Engineering Applications of Computational Fluid Mechanics

ISSN: 1994-2060 (Print) 1997-003X (Online) Journal homepage: www.tandfonline.com/journals/tcfm20

Modeling Monopile Scour in a Tidal-Dominated Coastal Sea: a GFD-CFD coupled framework and real-world application

Jialin Pang , Zaiyang Zhou , Xiaodao Wei & Jianzhong Ge

To cite this article: Jialin Pang , Zaiyang Zhou , Xiaodao Wei & Jianzhong Ge (2026) Modeling Monopile Scour in a Tidal-Dominated Coastal Sea: a GFD-CFD coupled framework and real-world application, Engineering Applications of Computational Fluid Mechanics, 20:1, 2696654, DOI: 10.1080/19942060.2026.2696654

To link to this article: https://doi.org/10.1080/19942060.2026.2696654

Published online: 02 Jul 2026.

ENGINEERING APPLICATIONS OF COMPUTATIONAL FLUID MECHANICS
2026, VOL. 20, NO. 1, 2696654
https://doi.org/10.1080/19942060.2026.2696654

Modeling Monopile Scour in a Tidal-Dominated Coastal Sea: a GFD-CFD coupled framework and real-world application

Jialin Pang[a], Zaiyang Zhou[a], Xiaodao Wei[b,c] and Jianzhong Ge[a]

[a]State Key Laboratory of Estuarine and Coastal Research, East China Normal University, Shanghai, People's Republic of China; [b]Shanghai Investigation, Design & Research Institute Co., Ltd, Shanghai; [c]Yangtze Eco-Environment Engineering Research Center (Shanghai), China Three Gorges Corporation, Shanghai

ABSTRACT
Local scour around monopile foundations poses a critical challenge for offshore wind turbines in tidal–dominated coastal seas, where hydrodynamics span multiple scales from kilometre-scale tidal currents to metre-scale horseshoe vortices. Conventional standalone geophysical fluid dynamics (GFD) or computational fluid dynamics (CFD) numerical modelling approaches struggle to resolve these cross-scale dynamics with sufficient accuracy and computational efficiency. To address this gap, this study extended GFD–CFD coupling from hydrodynamic simulations to sediment transport and scour morphodynamics modelling by integrating the unstructured-grid Finite-Volume Community Ocean Model (FVCOM) with the two-phase sediment transport solver SedFoam. This framework enables monopile scour to be simulated under realistic, time-varying tidal forcing, including flow reversal and rotation. The framework was first validated against laboratory flume experiments under bidirectional currents, reproducing scour evolution with RMSE values below 0.1 S/D (ratio of scour depth to monopile diameter). An idealized rotating tide experiment further showed that near-circular scour hole morphology was reproduced under flow with constantly varying direction. In a real-world application to Laizhou Bay, China, the simulated scour and deposition patterns around the monopile closely matched single–beam sonar surveys. The results suggest that tidal current direction, not residual circulation, governs scour orientation, highlighting the importance of realistic tidal forcing in scour modelling. The coupled framework provides a transferable tool for mechanistic and engineering assessments of monopile scour under complex coastal hydrodynamics.

ARTICLE HISTORY
Received 14 April 2026
Accepted 25 June 2026

KEYWORDS
Coupled modelling framework; Scour simulation; tidal currents; offshore monopile foundations; FVCOM; OpenFOAM

1. Introduction

In recent years, the construction of offshore infrastructure, such as cross-sea bridges and offshore wind farms, has accelerated in response to expanding human activities and rising energy demand in marine environments (Lemasson et al., 2024; Wang, Wang, et al., 2024). Offshore wind farms (OWFs) and offshore wind turbines (OWTs) constitute a large proportion of offshore infrastructure (Zhang, Tian, et al., 2021). Circular monopile foundations remain the predominant support type for offshore wind turbines (Guan et al., 2022; Jindal et al., 2024). A major engineering concern is local scour and backfilling around monopiles, which can compromise foundation stability and increase maintenance demands over the service life (Dai et al., 2021; Guo et al., 2022). In many offshore and coastal areas, scour relevant hydrodynamics are dominated by tides and their interaction with waves and background circulation (Geng et al., 2024; Kazhyken et al., 2021; Niedoroda & Dalton, 1982; Qin et al., 2024; Tang et al., 2014), highlighting the need for modelling tools that can provide realistic large-scale boundary forcing while resolving near field sediment dynamics.

A key challenge for engineering prediction is that tidal currents in coastal and nearshore regions constantly vary in both magnitude and direction. The horizontal velocity commonly follows a tidal-current ellipse and rotates over the dominant tidal period (Kopte et al., 2022; Vindenes et al., 2018). This directional variability, together with tidal asymmetry and phase lags between flow and sediment response, can shift the timing of erosion and deposition and yield a non-zero tidally averaged sediment transport (Chernetsky et al., 2010; Friedrichs & Aubrey, 1988). Although many monopile scour studies conducted under idealized unidirectional currents or wave–current interactions can reproduce scour patterns, they often neglect tidal forcing (e.g. Ahmad et al., 2015; Huang et al., 2009; Solberg et al., 2005). Even when tidal

CONTACT Jianzhong Ge jzge@sklec.ecnu.edu.cn State Key Laboratory of Estuarine and Coastal Research, East China Normal University, Shanghai 200241, People's Republic of China

effects are considered, some experiments are simplified as sinusoidal reciprocating flows (Shi-Yang et al., 2021) rather than realistic tidal ellipses.

A reciprocating tidal flow is a simplification that the current oscillates along a fixed axis. A real tidal current, by contrast, rotates continuously around a tidal ellipse. Therefore, the bed shear stress acts on the pile from all directions over a tidal cycle, so that the horseshoe vortex and the resulting erosion are redistributed around the structure rather than confined to two opposing sides (Whitehouse et al., 2006, 2011). At the same time, the absence of a quiescent state during reversal keeps the near-bed flow active and prevents the bed from reconsolidating between half cycles (Allen & Kudrolli, 2018; Clark et al., 2015), which alters the threshold for sediment remobilization. The interaction of such rotating tidal currents with complex topography and high suspended sediment concentrations further complicates the near-bed hydrodynamics (Li et al., 2024). Recent numerical studies also showed that tidal forcing plays an important role in regulating sediment suspension and transport in highly turbid coastal waters (Zhou et al., 2025). Field observations under irregular tidal flow further show that scour holes around coastal foundations can exhibit asymmetric morphology and frequent depth fluctuations, highlighting the complexity of flow–sediment interactions in real tidal environments (Zhang, Du, et al., 2023). Consequently, real-world flow–sediment interactions and scour morphology may not be fully captured by reciprocating-flow simplifications.

Flume experiments and numerical simulations are the two principal approaches to investigate scour around offshore infrastructure (Barrie et al., 2024; Wang, Wu, et al., 2024; Zhao, 2022). Recent flume studies have acknowledged that the hydrodynamic conditions experienced by monopile structures are neither constant nor unidirectional (Guan et al., 2022) and have explored reciprocating tidal forcing (Margheritini et al., 2006; Wang, Qi, et al., 2024; Xiang et al., 2020). These experiments revealed periodic scouring and backfilling. They also showed that bidirectional forcing can produce different scour depths and patterns compared with unidirectional flows. Nonetheless, flume experiments remain constrained by scale effects and inherent uncertainties (Hu et al., 2022; Lamb et al., 2015). Large-scale hydrodynamic processes, such as rotating tidal currents and ocean residual circulation, are inadequately represented in flume experiments. This limitation restricts their ability to consider complex interactions between hydrodynamics and sediment transport around offshore monopile infrastructure.

A growing number of numerical models have been developed to simulate the complex interactions between hydrodynamics and sediment transport. Geophysical fluid dynamics (GFD) models, such as Regional Ocean Modeling System (ROMS) and Finite-Volume Community Ocean Model (FVCOM), are widely used for long-term, large-scale simulations at $O(10^2 \sim 10^4\text{m})$, including tidal currents, ocean circulations and sediment transport (Pang et al., 2024; Qu et al., 2016; Tang et al., 2014). FVCOM has been applied to estuarine sediment transport and port-area suspended sediment simulations (Jia & Yi, 2023; Qi et al., 2023). The ROMS-based coupled modelling framework has also been used to assess sediment dynamics associated with estuarine dams and land reclamation, demonstrating its applicability to regional sediment-transport problems (Chang et al., 2023). These applications demonstrate that GFD models are effective for regional-scale hydrodynamic and sediment transport processes, but their ability to resolve local structure-induced scour remains limited by grid resolution and hydrostatic assumptions. For example, FVCOM can capture wake vortices around piles (Herdiansyah et al., 2019), yet horseshoe vortices remain difficult to resolve, partly because most GFD models neglect vertical acceleration (Wu & Tang, 2010).

In contrast, computational fluid dynamics (CFD) approaches solve the Navier–Stokes equations at high spatial resolution and are more suitable for resolving small-scale dynamic processes at $O(10^{-1} \sim 10^1\text{m})$ (Zhao et al., 2018), including near-bed turbulence, sediment entrainment and local scour around engineering structures. Such CFD approaches are implemented through various open-source codes and commercial softwares. For example, OpenFOAM is an open-source CFD toolbox containing multiple solvers for different flow applications, such as pimpleFoam for local hydrodynamic simulations (Weller et al., 1998). SedFoam is an OpenFOAM-based Eulerian two-phase solver specifically developed for sediment transport, flow–sediment interaction and scour modelling (Chauchat et al., 2017), and has been applied to apron scour, pipeline scour (Mathieu et al., 2019) and monopile scour (Nagel et al., 2020) simulations. Another CFD-based framework, REEF3D, has also been used for monopile scour, with improved efficiency through partial decoupling of hydrodynamic and morphological time scales (Ahmad et al., 2018). Nevertheless, these CFD-based simulations remain computationally expensive for realistic large-scale forcing and long durations, limiting their direct application to offshore environments.

To balance large-scale hydrodynamic forcing with small-scale flow–sediment resolution, GFD-CFD coupled modelling frameworks provide a practical approach. Growing efforts have been applied to the coupled GFD and CFD models around offshore infrastructure (Alvir et al., 2022; Lu et al., 2024; Pang et al., 2024; Paulsen et al., 2014; Qu et al., 2019; Tang et al., 2014; Wu & Tang, 2010; Zhang, Wang, et al., 2023). However, existing studies mainly focused on the hydrodynamics simulation, with the seabed treated as a fixed boundary. As a result, scour morphodynamics under realistic, time-varying tidal forcing has not been addressed within a cross-scale coupled framework.

In this study, the existing GFD–CFD framework is extended from hydrodynamic simulation to sediment transport and scour morphodynamics modelling. This extension is achieved by coupling FVCOM with SedFoam, building on the framework of Pang et al. (2024). FVCOM provides realistic regional tidal forcing, whereas SedFoam resolves local scour evolution around the monopile. The model is further evaluated under time-varying tidal forcing, including flow reversal and rotation.

This study focuses on circular monopile foundations, the most widely adopted support type for OWTs (Guan et al., 2022; Hou et al., 2022; O'Kelly & Arshad, 2016). The remainder of this paper is organized as follows. Section 2 presents the coupling framework for GFD and CFD models. The validation of the coupled modelling framework is given in Section 3. The testing results of idealized simulations are presented in Section 4. In Section 5, the practical application of the proposed modelling framework to an offshore wind farm is introduced. Insights and general perspectives on this coupled modelling framework are discussed in Section 6, and conclusions are summarized in Section 7.

2. Models and methodology

2.1. GFD model: FVCOM

The GFD model applied in the coupling framework is the Finite-Volume Community Ocean Model (FVCOM), a three-dimensional prognostic primitive equation model based on an unstructured triangular grid framework (Chen et al., 2003). It employs a generalized terrain-following coordinate system (Pietrzak et al., 2002) for vertical discretization, allowing adaptive resolution of bathymetric variations. The unstructured mesh allows accurate fitting of irregular geometries and flexible grid refinement. FVCOM incorporates the Mellor-Yamada 2.5-level turbulence closure model for vertical mixing (Mellor & Yamada, 1982) and the Smagorinsky formulation (Smagorinsky, 1963) as the default horizontal diffusion scheme.

The governing equations include the momentum equations (Equations (1)-(3)), the continuity equation (Equation (4)), the hydrostatic term in the momentum equation (Equation (5)), the temperature equation (Equation (6)), the salinity equation (Equation (7)), and the density equation (Equation (8)):

$$\frac{\partial u}{\partial t} + u\frac{\partial u}{\partial x} + v\frac{\partial u}{\partial y} + w\frac{\partial u}{\partial z} - fv = -\frac{1}{\rho_0}\frac{\partial P_H + P_a}{\partial x} - \frac{1}{\rho_0}\frac{\partial q}{\partial x} + \frac{\partial}{\partial z}\left(K_m\frac{\partial u}{\partial z}\right) + F_u, \tag{1}$$

$$\frac{\partial v}{\partial t} + u\frac{\partial v}{\partial x} + v\frac{\partial v}{\partial y} + w\frac{\partial v}{\partial z} + fu = -\frac{1}{\rho_0}\frac{\partial P_H + P_a}{\partial y} - \frac{1}{\rho_0}\frac{\partial q}{\partial y} + \frac{\partial}{\partial z}\left(K_m\frac{\partial v}{\partial z}\right) + F_v, \tag{2}$$

$$\frac{\partial w}{\partial t} + u\frac{\partial w}{\partial x} + v\frac{\partial w}{\partial y} + w\frac{\partial w}{\partial z} = -\frac{1}{\rho_0}\frac{\partial q}{\partial z} + \frac{\partial}{\partial z}\left(K_m\frac{\partial w}{\partial z}\right) + F_w, \tag{3}$$

$$\frac{\partial u}{\partial x} + \frac{\partial v}{\partial y} + \frac{\partial w}{\partial z} = 0, \tag{4}$$

$$P_H = \rho_0 g\zeta + g\int_z^0 \rho\, dz, \tag{5}$$

$$\frac{\partial T}{\partial t} + u\frac{\partial T}{\partial x} + v\frac{\partial T}{\partial y} + w\frac{\partial T}{\partial z} = \frac{\partial}{\partial z}\left(K_h\frac{\partial T}{\partial z}\right) + F_T, \tag{6}$$

$$\frac{\partial S}{\partial t} + u\frac{\partial S}{\partial x} + v\frac{\partial S}{\partial y} + w\frac{\partial S}{\partial z} = \frac{\partial}{\partial z}\left(K_h\frac{\partial S}{\partial z}\right) + F_S, \tag{7}$$

$$\rho = \rho(T, S, p), \tag{8}$$

where in the Cartesian coordinate system, velocity components are denoted as u (eastward), v (northward), and w (vertical). Additional variables include temperature (T), salinity (S), and water density (ρ). Pressure terms consist of atmospheric pressure at sea level (P_a), hydrostatic pressure (P_H), non-hydrostatic pressure (q). Other parameters include the Coriolis parameter (f), gravitational acceleration (g), vertical eddy viscosity coefficient (K_m), and thermal vertical eddy diffusion coefficient (K_h). Horizontal momentum, temperature, and salinity diffusion terms in the u and v directions are represented as F_u, F_v, F_T and F_S, respectively. The total pressure (P) is defined as the sum of atmospheric, hydrostatic, and non-hydrostatic pressures ($P = P_a + P_H + q$). Since this study adopts the hydrostatic assumption, the non-hydrostatic pressure is set to $q = 0$, reducing the total pressure is $P = P_a + P_H$. The total water depth is given by $D = H + z$ where H is the bottom depth relative to the reference level $z = 0$ and z represents the height of the free surface ($z = 0$).

In particular, in a previous study (Pang et al., 2024), it was incorporated to simulate cross-scale flow dynamics around offshore monopile foundations. FVCOM model configurations adopted in this study follow Pang et al. (2024).

2.2. CFD model: OpenFOAM and sedfoam

The CFD modelling component of this study uses OpenFOAM, an open-source software tool that offers a set of solvers for fluid simulations (Weller et al., 1998). Seabed morphological changes and sediment transport are calculated using the SedFoam solver, a three-dimensional two-phase sediment transport solver (Chauchat et al., 2017). SedFoam is an extension of the twoPhaseEulerFoam solver in OpenFOAM that provides a number of options for modelling intergranular stress based on dense granular-flow rheology or the kinetic theory of granular flows. It has proven to be effective in solving complicated turbulent sediment transport problems through extensive testing and validations (Cheng et al., 2018; Salimi-Tarazouj et al., 2021).

The mass and momentum conservation equations are averaged over the fluid and sediment phases using the Eulerian two-phase flow method, incorporating turbulent effects. For both the sediment and fluid phases, the mass conservation equations are expressed as follows:

$$\frac{\partial \alpha}{\partial t} + \frac{\partial \alpha u_i^a}{\partial x_i} = 0, \tag{9}$$

$$\frac{\partial \beta}{\partial t} + \frac{\partial \beta u_i^b}{\partial x_i} = 0, \tag{10}$$

where α and β ($\beta = 1 - \alpha$) represent the sediment and fluid volume concentrations, respectively. The velocities of the sediment and fluid phases are denoted as u^a and u^b, where $i = 1,2,3$ are the streamwise, spanwise, and vertical components. The momentum equations for the suspended sediment and fluid phases are given as follows:

$$\frac{\partial \rho^a \alpha u_i^a}{\partial t} + \frac{\partial \rho^a \alpha u_i^a u_j^a}{\partial x_j} = -\alpha \frac{\partial p}{\partial x_i} + \alpha f_i - \frac{\partial \widetilde{p^a}}{\partial x_i} + \frac{\partial \tau_{ij}^a}{\partial x_j} + \alpha \rho^a g_i + \alpha \beta K (u_i^b - u_i^a) - S_{US} \beta K \nu_t^b \frac{\partial \alpha}{\partial x_i}, \tag{11}$$

$$\frac{\partial \rho^b \beta u_i^b}{\partial t} + \frac{\partial \rho^b \beta u_i^b u_j^b}{\partial x_j} = -\beta \frac{\partial p}{\partial x_i} + \beta f_i + \frac{\partial \tau_{ij}^b}{\partial x_j} + \beta \rho^b g_i - \alpha \beta K (u_i^b - u_i^a) + S_{US} \beta K \nu_t^b \frac{\partial \alpha}{\partial x_i}, \tag{12}$$

where ρ^a and ρ^b denote the densities of sediment and fluid, respectively. The gravitational acceleration is represented by g_i, while f_i is an external volume force driving the flow. The fluid pressure is given by p, and the fluid stress τ_{ij}^b includes both fluid grain-scale stress and fluid Reynolds stresses. The partial normal and shear stresses are denoted as $\widetilde{p^a}$ and τ_{ij}^a, respectively. The drag parameter is represented by K, the turbulent viscosity by ν_t^b, and S_{US} is the inverse of the Schmidt number.

Turbulence modelling is required to account for the unresolved Reynolds stresses. The momentum equations presented above are the phase-averaged governing equations for the Eulerian two-phase system. The Reynolds-Averaged Navier–Stokes (RANS) formulation is introduced as a closure approach for the Reynolds-stress contribution in the fluid stress tensor. In the present model, these turbulent stresses are closed using the two-phase $k - \omega$ model implemented in SedFoam.

Following Chauchat et al. (2017), the turbulent eddy viscosity is calculated as

$$\nu_t^b = \frac{k}{\omega}, \tag{13}$$

and the transport equations for the fluid-phase turbulent kinetic energy k and the specific dissipation rate ω are

$$\frac{\partial k}{\partial t} + u_j^b \frac{\partial k}{\partial x_j} = R_{ij}^{bt} \frac{\partial u_i^b}{\partial x_j} + \frac{\partial}{\partial x_j}\left[\left(\nu^b + \frac{\nu_t^b}{\sigma_k}\right)\frac{\partial k}{\partial x_j}\right] - C_\mu k \omega - \frac{2K(1 - t_{mf})\alpha k}{\rho^b} - \frac{S_{US}}{\beta} \nu_t^b \frac{\partial \alpha}{\partial x_j}\left(\frac{\rho^a}{\rho^b} - 1\right) g_j, \tag{14}$$

$$\frac{\partial \omega}{\partial t} + u_j^b \frac{\partial \omega}{\partial x_j} = C_{1\omega} \frac{\omega}{k} R_{ij}^{bt} \frac{\partial u_i^b}{\partial x_j} + \frac{\partial}{\partial x_j}\left[\left(\nu^b + \frac{\nu_t^b}{\sigma_\omega}\right)\frac{\partial \omega}{\partial x_j}\right] - C_{2\omega}\omega^2 - C_{3\omega}\frac{2K(1 - t_{mf})\alpha \omega}{\rho^b} - C_{4\omega} S_{US} \frac{\omega}{k\beta} \nu_t^b \frac{\partial \alpha}{\partial x_j}\left(\frac{\rho^a}{\rho^b} - 1\right) g_j, \tag{15}$$

where the Reynolds stress tensor is given by $R_{ij}^{bt} = \rho^b \beta \left[2\nu_t^b S_{ij}^b - \frac{2}{3} k \delta_{ij}\right]$ with S_{ij}^b being the deviatoric part of the fluid-phase strain-rate tensor. $t_{mf} = \exp(-BSt)$ represents the correlation between sediment and fluid velocity fluctuations, the coefficient B is treated as the only free calibration parameter, consistent with the practice of Chauchat et al. (2017). The last two terms in Equations (14) and (15) account for the two-phase effects associated with sediment-induced drag damping and sediment-induced density stratification. The default coefficients are $C_\mu = 0.09$, $C_{1\omega} = 5/9$, $C_{2\omega} = 3/40$, $C_{3\omega} = 0.35$, $\sigma_k =$

$\sigma_\omega = 2.0$, and $S_{US} = 1.0$. The coefficient $C_{4\omega}$ is set to 0 for stable stratification and 1 for unstable stratification.

By introducing sediment-induced drag and turbulence suspension terms into the clear-water $k-\omega$ model equations, corrections are applied to the fluid-phase turbulent kinetic energy (TKE) and specific dissipation rate (ω) equations.

2.3. Coupling method

The overall framework is presented in Figure 1. FVCOM, as the GFD model, resolves the time-varying and large-scale hydrodynamics over the entire OWF area, including tidal currents and regional circulations. The CFD model OpenFOAM uses FVCOM outputs as boundary forcing to capture small-scale turbulence and local scour around a single OWT. A common-boundary nesting strategy integrates GFD and CFD models by leveraging their strengths. This method aligns FVCOM's unstructured triangular mesh with OpenFOAM's structured grid at a shared boundary to ensure accurate momentum flux consistency. FVCOM velocities are mapped from the unstructured triangular mesh onto the OpenFOAM boundary faces using horizontal interpolation on the nesting area and vertical profile reconstruction following the fifth-order fitting procedure of Pang et al. (2024). In the present framework, FVCOM is used to provide regional hydrodynamic forcing, whereas local sediment transport and bed evolution around the monopile are resolved by SedFoam. Therefore, only the time-varying velocity field is transferred from FVCOM to SedFoam through the nesting boundary. The mass and momentum transfer at the nesting interface follows the common-boundary nesting method previously validated by Pang et al. (2024), in which the interface velocity distribution and the full interface section were examined to verify the consistency of FVCOM–OpenFOAM coupling. The present study adopts the same validated interface treatment and extends it from hydrodynamic downscaling to two-phase sediment transport and scour simulation.

The framework dynamically updates flow directions and velocities at each time step, with OpenFOAM boundary conditions adaptively adjusted based on flux direction. Specifically, the *inletOutlet* boundary condition is used at the lateral boundaries, where a fixed velocity and *zeroGradient* pressure are specified at the inlet, and *zeroGradient* velocity and fixed-value pressure are applied at the outlet. The bottom boundary and the monopile use wall functions to accurately represent near-wall turbulence.

By confining CFD simulations to the near-field region around infrastructures and using parallel computing, the nesting strategy effectively captures critical cross-scale

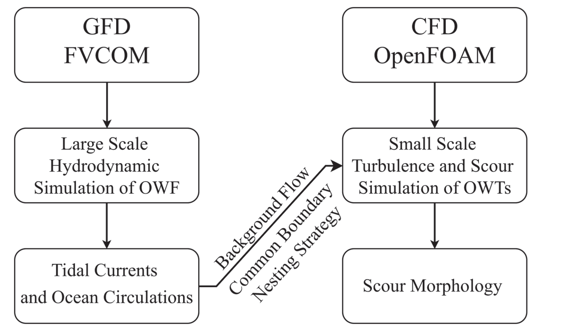

Figure 1. Schematic of the FVCOM–OpenFOAM modelling framework.

flow dynamics, such as wake and vortex formation. The parameter settings for sediment properties and transport processes follow the formulations of Chauchat et al. (2017). Given the localized impact of scour around individual pile foundations, sediment distribution and characteristics are simplified to be uniform to reduce model complexity and maintain computational efficiency. Both FVCOM and SedFoam are initialized with zero velocity, and the coupled modelling framework undergoes a gradual transition to realistic flow conditions over a ramp period of one hour. More detailed information about this one-way coupling between GFD and CFD models, as well as data transfer methods and the mass-conservation validation, can be found in Pang et al. (2024).

3. Validations

Two validation cases were conducted to assess model performance under time-varying, non-unidirectional forcing, with emphasis on the boundary handling during flow reversal and the resulting scour response. First, a three-dimensional (3-D) monopile case from Schendel et al. (2018) is used to validate the temporal evolution of scour depth under reciprocating flow. Second, a two-dimensional (2-D) case based on bidirectional-current flume experiments for a submarine pipeline (Zhang, Guo, et al., 2021) is used to evaluate erosion–deposition morphology. It should be noted that, in the present two-phase Eulerian formulation, neither an explicit critical shear stress nor an empirical erosion coefficient is prescribed. Bed mobilization and sediment fluxes arise from the resolved phase-momentum balance coupled with the granular rheology and particle-pressure closures. Likewise, an explicit settling velocity w_s is not imposed as a model input. The effective settling behaviour emerges from the two-phase momentum equations and is controlled by the interphase momentum-exchange closure, together with the specified sediment and fluid properties. Case-dependent parameters were specified in Table 1. All

Table 1. Sediment parameters used in the validation and idealized case.

Case	d50 (mm)	Hindrance exp.	Shape factor	Particle-stress closure	Granular rheology	Interphase drag model
3-D monopile validation	0.19	2.65	0.7	Johnson–Jackson	μ(I) + Johnson–Jackson	Gidaspow–Schiller–Naumann
2-D pipline validation	0.15	2.65	0.9			
3D idealized monopile rotating tide	0.26	2.65	1.0			

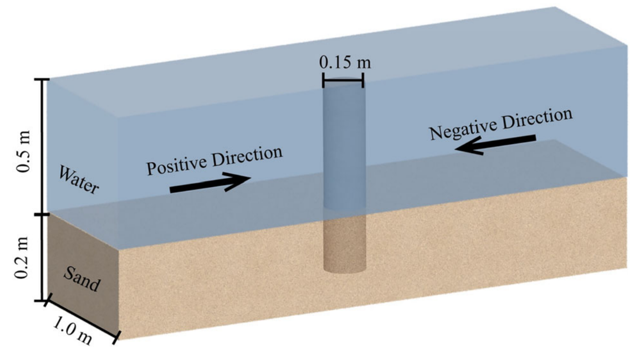

Figure 2. The flume experiment setup. The monopile has a diameter of 0.15 m and is centrally positioned in a 1.0 m-wide tank with a 0.2 m-thick sand bed and 0.5 m water depth. The flow alternates between the positive and negative directions to simulate tidal currents.

SedFoam closure coefficients follow the default settings of Chauchat et al. (2017).

3.1. 3-D time-varying scour depth validation

Bidirectional and rotating tidal currents can produce complex erosion and deposition patterns around offshore structures, motivating validation under non-unidirectional forcing. Temporal variations in scour depth are of great significance, offering valuable guidance for planning and maintaining protective measures for foundations during the operational phase of offshore wind turbines. The 3-D monopile simulation is therefore validated against the bidirectional flow flume experiments of Schendel et al. (2018). The flume experiment setup is shown in Figure 5. The monopile diameter is $D = 0.15$m, and the sediment has $d_{50} = 0.19$mm and the density $\rho_s = 2650$kg/m^3. The water depth is 0.5 m, with an initial sediment bed thickness of 0.2 m (Figure 2). The same particle-stress closure as in Section 3.1 is used. In this case, $s_F = 0.7$ and $h_{\text{exp}} = 2.65$ (Table 1).

Local refinement is also applied around the monopile, achieving a resolution $\Delta x = 0.004$m (Figure 3(a)). In the vertical direction, the grid is discretized into 110 layers, with the finest resolution $\Delta z = 0.003$m near the water-sediment interface (Figure 3(b)). The time step is 0.05 s. The simulation is initialized from rest with clear water, following the flume configuration in Schendel et al. (2018).

The temporal evolution of scour depths at three locations on the upstream, downstream and lateral sides of the pile foundation was extracted to compare with the flume experiment (Figure 3(a)). The point at (−0.1,0) is denoted as the upstream point for the positive-flow phase, the point at (0.1,0) as the downstream point for the negative-flow phase, and the point at (0,0.1) as the lateral point. Tidal currents are idealized as regular sinusoidal flows with a maximum velocity of 0.45 m/s and a period of 117 min (Figure 4(a)).

During the first 6 min, the flow was too weak to produce measurable bed change, and S/D (normalized scour depth, i.e. ratio of scour depth to pipeline diameter) remained close to zero at both points (Figure 4(b)). Scour at the upstream point became evident by the 12th min, increasing from S/D = 0.1 to 0.88 by the 33rd min. As the velocity began to decrease, the S/D value stabilized and stopped increasing. The lateral point exhibits a similar increasing trend to the upstream point between 12 and 33 min, with S/D rising rapidly as the positive flow strengthen. By the 33rd min, S/D at the lateral point reached approximately 0.78 and then remained nearly stable.

Under the same positive flow phase, the downstream point also exhibited a scour trend, but with a smaller maximum scour depth than at the upstream point. Scour became evident after 21 min and reached S/D = 0.52 by the 33rd min, after which it remained nearly constant as the flow weakened. The smaller scour depth at the downstream point is attributed to wake-induced flow reduction and sediment settling in the lee side of the monopile. The flume data further show a depositional phase at the downstream point between the 12th and the 21st min, which is not reproduced by the model, potentially due to the simplified sediment representation.

Between the 60th and 78th minute, the largest discrepancy occurred at the upstream and lateral point (blue-shaded region in Figure 4(b)). Between 60 and 78 min, the simulated scour depth decreases from S/D = 0.85 to 0.60 at the upstream point and from S/D = 0.78 to 0.55 at the lateral point, whereas the flume measurements show only a slight decrease of approximately 0.05 S/D. At the downstream location, both model simulation and flume experiment show continuous scour, the numerical model

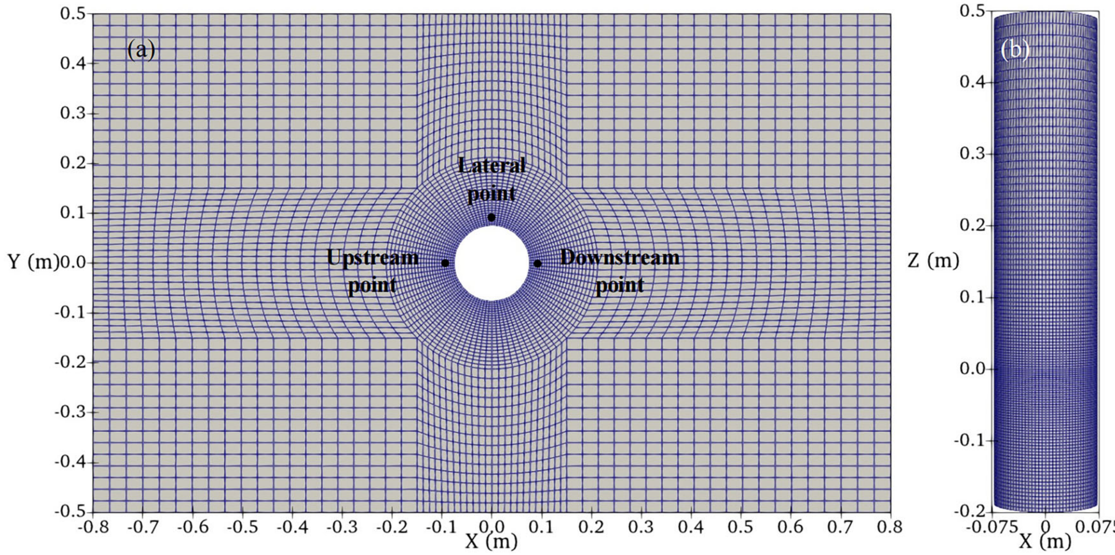

Figure 3. Model grids in the horizontal (a) and vertical (b) direction for 3-D time-varying scour depth validation. Three black dots indicate locations selected for validation in the positive, negative flow directions and lateral point.

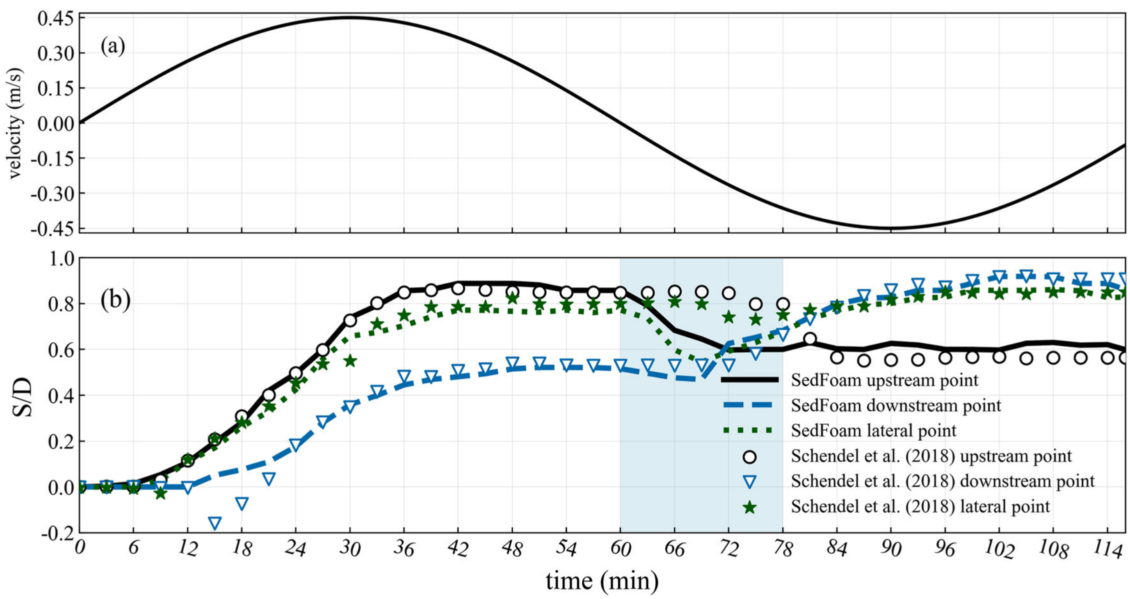

Figure 4. (a) The flume experiment and model velocity variation. The positive velocity represents the direction of incoming flow, and the corresponding validation point for positive velocity is noted as the upstream point in Figure 3. (b) Comparison of S/D at the upstream, downstream and lateral monitoring points around the monopile. The black solid, blue dashed and green dotted lines denote SedFoam results, while the black circles, blue triangles and green stars denote the corresponding experimental measurements. S/D represents the ratio of scour depth to monopile diameter. The shaded blue area highlights regions with the largest discrepancies between the model and experimental results.

increases from S/D = 0.51 to 0.68, while the flume experiment increases from S/D = 0.53 to 0.66, suggesting a high degree of consistency.

The discrepancy at the upstream point is mainly attributed to the difference in flow reversal treatment between the numerical model and the flume experiment. The flow forcing in numerical model is a continuous sinusoidal velocity, enabling uninterrupted sediment transport throughout the entire simulation. In the flume, however, the bidirectional current was implemented as separate phases with a stop–restart procedure before reversing direction. Consequently, this introduces a quiescent transition period during which suspended sediment settles, the bed reorganizes and reestablishes granular structure before the next phase begins (Allen & Kudrolli, 2018). Such bed reorganization may increase the resistance to remobilization, so restarting sediment motion can require a higher shear stress than sustaining ongoing transport (Clark et al., 2015). During flow reversal, the lateral region is sensitive to the redistribution of near-bed shear and vortical structures. Previous oscillatory-flow studies around vertical cylinders have shown that horseshoe and wake vortices can strongly affect bed shear stress and sediment entrainment around the cylinder (Chang & Constantinescu, 2023).

While this explains the deviations during flow reversal, the continuous forcing used in the numerical model is more representative of real coastal tidal environments than a fully interrupted phase-segmented forcing. In natural tidal flows, background currents, residual motion and turbulence can persist through flow reversal, rather than allowing the bed to return to a fully quiescent state.

Overall, the model achieved good agreement with the flume experiment in reproducing the temporal variation of scour depth on both the upstream and downstream sides of the monopile under reciprocating flow conditions, with RMSE values of 0.08 and 0.05 S/D at the upstream and downstream points, respectively.

3.2. 2-D scour shape validation

The bidirectional pipeline flume experiment of Z. Zhang et al. (2021) is used as a 2-D benchmark for scour-shape validation. The pipeline diameter is $D = 0.045$m and the sediment median grain size $d_{50} = 0.15$mm and density $\rho_s = 2650$kg/m^3. The water depth is 0.5 m with an initial bed thickness of 0.2 m (Figure 5(a)). Tidal currents in this experiment are simplified as standard sinusoidal signals, with a maximum flow velocity of 0.3 m/s and a period of 2.68 h (Figure 5(b)). SedFoam is configured with a dense granular rheology combining a μ(I)-type friction law with a Johnson–Jackson particle-pressure closure (Table 1). The drag shape factor $s_F = 0.9$ and a hindrance exponent $h_{\text{exp}} = 2.65$.

The computational grid is shown in Figure 6a, with local refinement on both sides of the pipeline and near the water-sediment interface (Figure 6(b)). The near-pipeline mesh resolution is $\Delta x = 1.0 \times 10^{-3}$ m and $\Delta z = 2.0 \times 10^{-4}$ m, with a timestep set to 10^{-3} s. To match the 2-D benchmark configuration and reduce computational cost, the simulation is performed on an x–z plane (2-D).

Scour patterns around the submarine pipeline were analysed and compared at the T/4 (Figure 7(a)) and 3 T/4 (Figure 7(b)) of the tidal cycle, corresponding to the flood maximum and ebb maximum, respectively. At T/4, the model agrees well with the measurements. Scour develops mainly beneath the pipeline and upstream, with S/D = 0.26 at maximum. Deposition forms downstream around X/D = 0.1, reaching a maximum height of 0.24 D. Bed-level change within the scour hole area matches the flume observations, with an RMSE of 0.05 S/D.

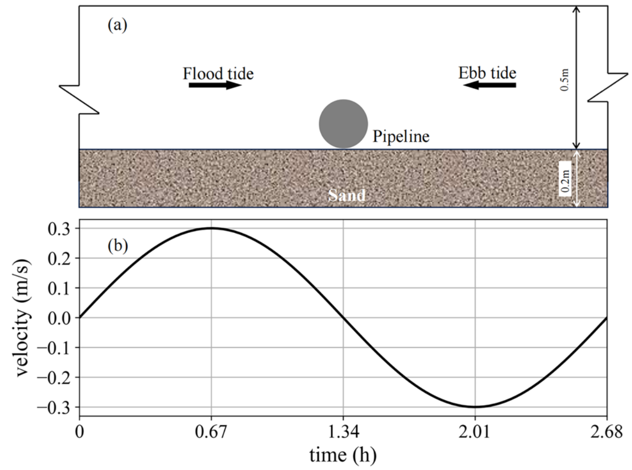

Figure 5. The flume experiment setup (a) and velocity setting (b). The positive velocity represents the flood tide, and the negative velocity corresponds to the ebb tide.

At 3 T/4, the scour pattern becomes nearly symmetric due to flow reversal, and the maximum scour depth beneath the pipeline increases to S/D = 0.28. The RMSE between the simulated and measured bed profiles within the scour hole area is 0.10 S/D. Overall, the model results exhibited good agreement with the flume experiments in terms of scour depth under bidirectional forcing.

However, discrepancies remain in the backfilling area. Similar behaviour was also reported by Mathieu et al. (2019) in SedFoam pipeline-scour simulations. The scour depth and scour hole shape were reproduced more reliably than the downstream bed response. This is mainly due to the limited representation of pipeline lee-wake turbulence–sediment interactions in two-phase RANS models. Overall, the model reproduced the dominant scour depth and scour extent under bidirectional flow conditions.

4. Idealized experiment of rotating tidal currents

4.1. Model setup

Previous validation has demonstrated the model's capability to simulate scour development around the monopile under bidirectional flows. However, most OWT foundations are located in environments where tidal currents rotate in direction over the tidal cycle (Margheritini et al., 2006). An idealized rotating-current case is therefore used to examine scour development under continuously varying flow direction.

A geometric scaling of 1:100 was adopted, such that the prototype monopile diameter of 10 m was reduced to

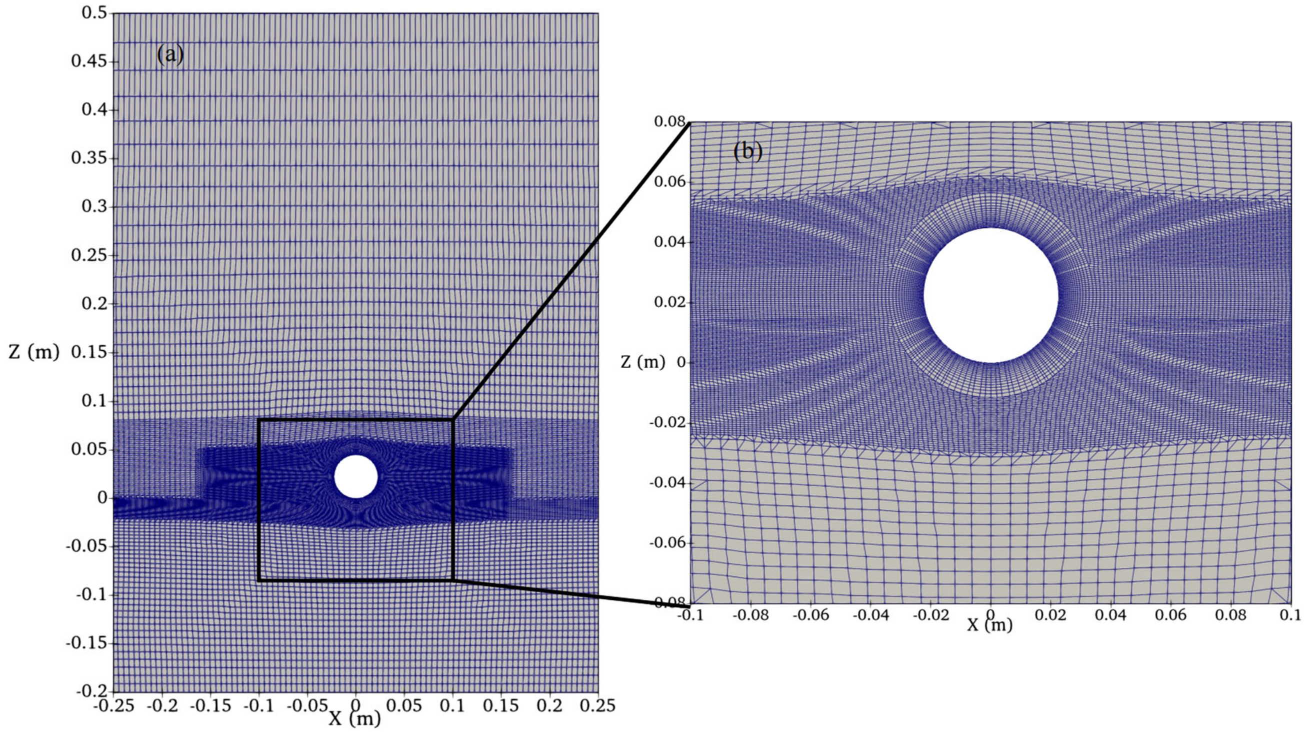

Figure 6. Model grids in the horizontal direction of the flume experiment for validation (a), and the enlarged view around the pipeline (b). The mesh resolution is 0.001 m horizontally and 0.0002 m vertically.

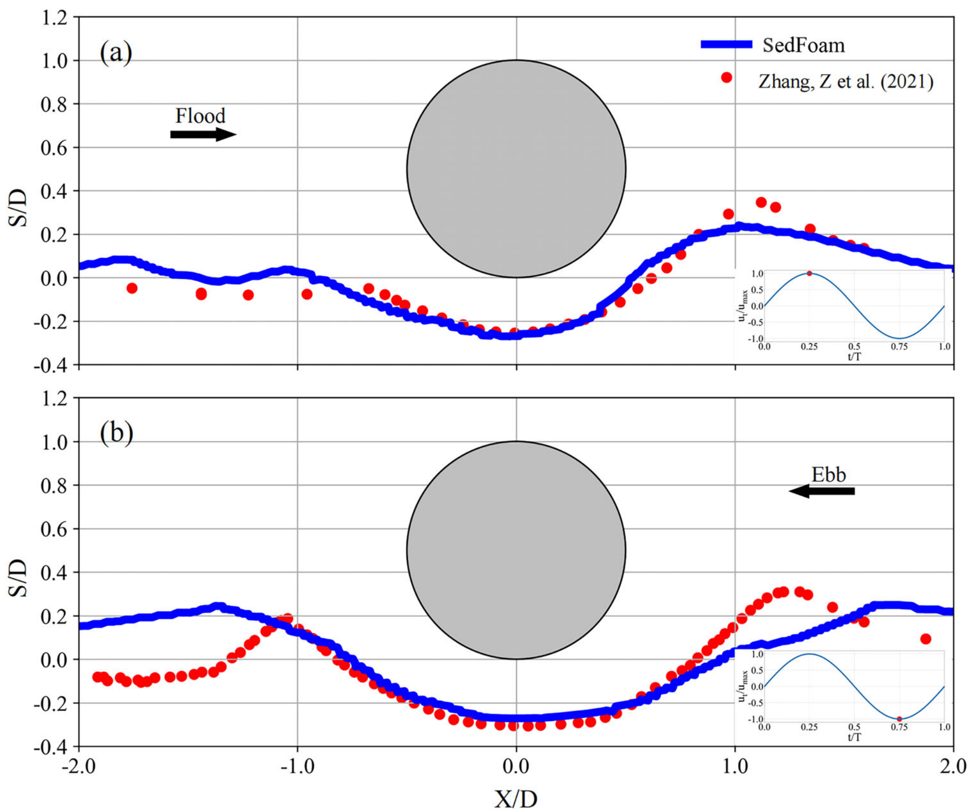

Figure 7. Scour validation under bidirectional flow conditions against the flume experiment of Z. Zhang et al. (2021) at 1/4 cycle (a) and 3/4 cycle (b). The inner panels and arrows indicate the corresponding flow magnitude and direction. X/D and S/D represent the normalized distance relative to the pipeline diameter in the horizontal and vertical plane, respectively.

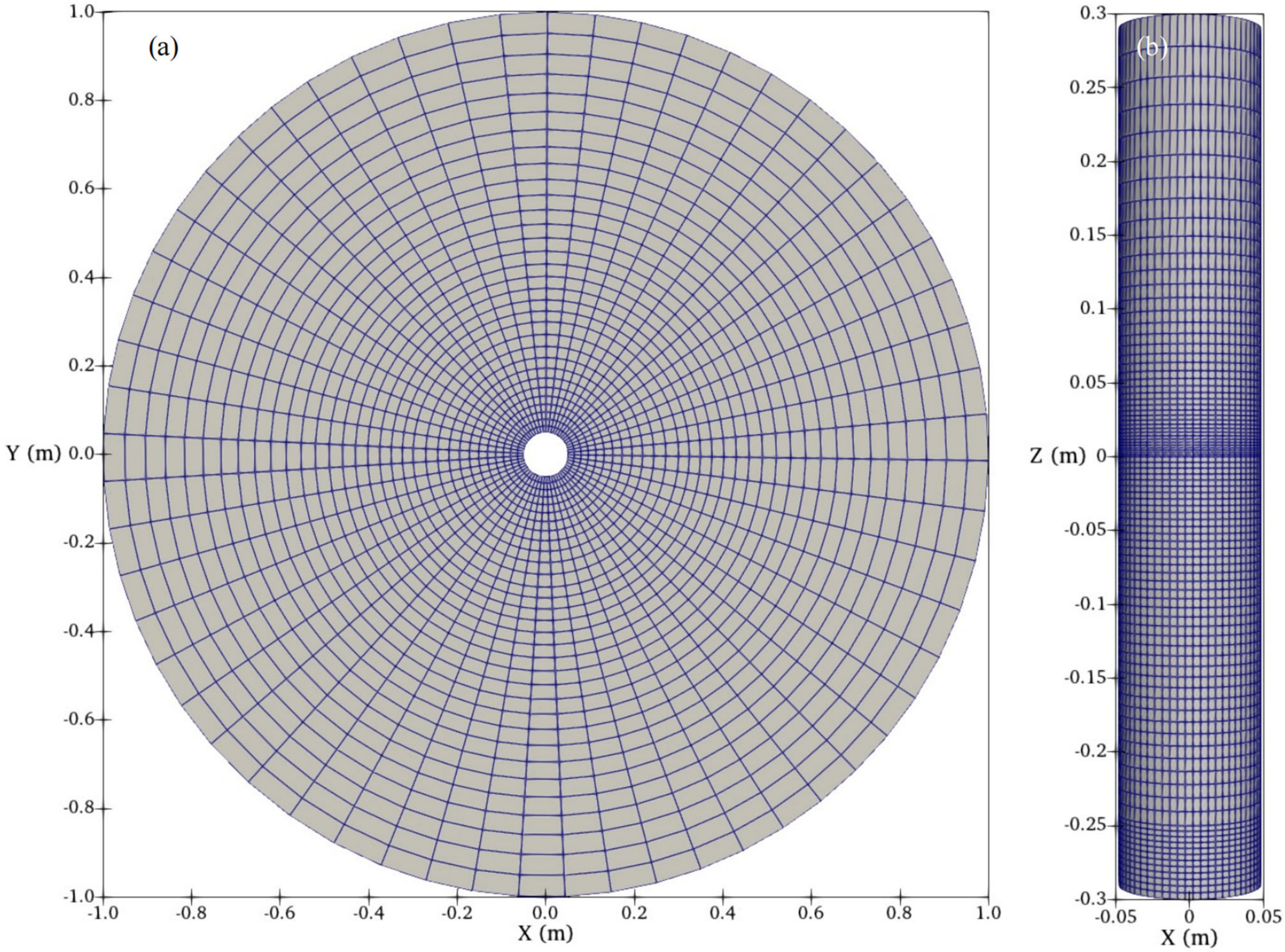

Figure 8. Model grids in the horizontal (a) and vertical (b) of the idealized experiment of 3-D flow-sediment interaction case.

$D = 0.1$m in the model. The computational domain was circular with radius $R = 1$m $(R/D = 10)$, and the water depth was set to $H = 0.3$m $(H/D = 3)$ (Figure 8(a)). The mesh resolution was $\Delta x = 0.01$m in the inner region and $\Delta x = 0.04$m in the outer region. The water column was discretized into 64 vertical layers with stretching, giving $\Delta z = 0.02$m near the free surface and a minimum $\Delta z = 0.001$m m near the bed–water interface. (Figure 8(b)).

To obtain obvious scour within one tidal cycle, a prototype maximum flow velocity of 2 m/s was selected, based on possible conditions during spring tides in the coastal waters of China (Wu et al., 2021). Using Froude scaling, the prototype velocity was scaled down to a spatially uniform current with a constant speed of 0.2 m/s. The resulting Froude number, defined as $Fr = U/\sqrt{gD}$, was $Fr = 0.20$. The rotating tide was imposed by prescribing two orthogonal, depth-uniform velocity components, $U_x(t) = 0.2\cos(\omega t)$ and $U_y(t) = 0.2\sin(\omega t)$, with $\omega = 2\pi/T_{M2}$ and $T_{M2} = 4471$s, giving a period of 1.24 h scaled from astronomical semi-diurnal tidal component M_2. The ramp time was extended by an additional 10 s to reduce spin-up transients in the coupled flow–sediment response.

In this idealized case, the sediment is represented as sand with a density of 2650 kg/m^3 and a median grain size of $d_{50} = 0.26$mm. The hindrance exponent 2.65 for concentration-dependent drag. Turbulence is modelled with the two-phase $k - \omega$ RANS closure. The particle-stress closure is the same as in the two validation cases.

4.2. Results of the idealized experiment

The rotating currents produced a strongly time-dependent scour morphology around the monopile. The model bathymetry was initially flat (Figure 9(a)). A horseshoe-shaped scour hole developed after 354 s of simulation due to the near-bed downflow and the increased bottom shear stress from vortex formation (Figure 9(b)). The scour depth could reach up to 0.3S/D. As the current direction rotated counter-clockwise, the horseshoe vortex and bottom shear stress evolved, driving dynamic changes in the scour hole's shape and development. From t = 354 s (Figure 9(b)) to t = 4481 s (Figure 9(f)), the scour hole

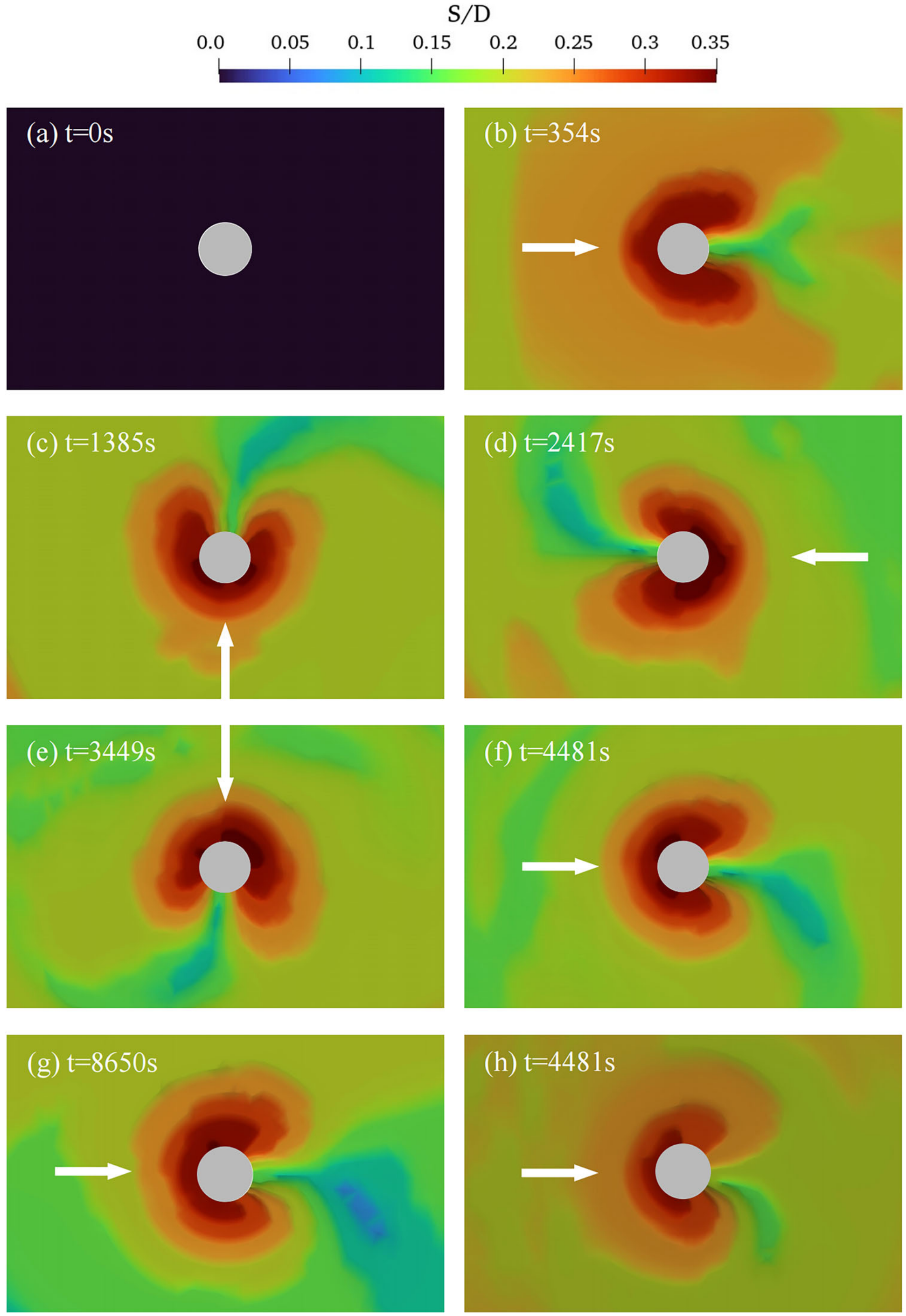

Figure 9. Scour pattern of idealized 3-D scour experiment at (a) t = 0 s, (b) t = 354 s, (c) t = 1385 s, (d) t = 2417 s, (e) t = 3449 s, (f) t = 4481 s. Panels (g) and (h) show the final scour pattern from the sensitivity analysis, where (g) is the case with the scaled S_1 period and (h) is the case with a coarser sediment ($\boldsymbol{d} = 0.5\text{mm}$). S/D represents the ratio of scour depth to monopile diameter. White arrows indicate the current direction.

became approximately circular around the monopile, and the downstream deposition was rotated following the instantaneous flow direction. The maximum scour depth gradually developed from 0.3 S/D to 0.35 S/D during this period. The intermediate stages of scour development are shown in Figures 9c–e.

A near-circular scour hole is also reported in field observations from areas with rotating tidal currents (Whitehouse et al., 2006, 2011). Unlike the symmetrical scour patterns commonly aligned with the dominant flow direction under unidirectional or reciprocating currents, the scour morphology under rotating tidal currents is different. Under rotating tidal currents, the current direction changes continuously, so bed shear varies around the pile over the cycle. This promotes erosion from multiple directions and gradually forms a more circular scour hole. By effectively integrating local CFD flow with large-scale GFD flow, the framework provides a valid approach to understanding scour dynamics.

To examine the sensitivity of the circular scour hole to current rotation speed and sediment grain size, two additional cases were conducted, including one using scaled diurnal astronomical component S_1 period of 8640s, with a total simulation time of 8650 s including a 10 s ramp time (Figure 9g) and one with a coarser sediment size ($d_{50} = 0.5$mm) (Figure 9h). Both cases still produce a circular scour hole. Compared with the M_2-scaled case, the S_1-scaled case shows nearly identical maximum scour depth and overall scour morphology. With the same velocity amplitude, the peak bed shear stress and Shields parameter remain unchanged, and the large flow excursion length ($L = UT$) allows the horseshoe-vortex and near-bed shear fields to develop sufficiently in both cases (Fredsøe and Sumer, 2002 ; Chang & Constantinescu, 2023). Therefore, changing the rotation period within the tested range has a limited influence on the maximum scour depth. In contrast, increasing d_{50} clearly reduces the scour depth, with a maximum scour depth of 0.31 S/D. According to the Shields parameter, $\theta = \tau_b/[(\rho_s - \rho_f)gd]$, a larger grain size reduces sediment mobility and increases the critical shear stress required for entrainment under the same hydrodynamic forcing (Shields, 1936; Van Rijn, 1984). Therefore, the coarser-sediment case produces a shallower scour hole, while the circular hole is still maintained under rotating forcing.

4.3. Comparison with standalone FVCOM

For comparison, a standalone FVCOM simulation was conducted using the same velocity forcing and sediment parameters as described in Section 4.1. As shown in Figure 10a, the FVCOM mesh was refined to a horizontal resolution of 0.02 m at the monopile, matching the resolution used in OpenFOAM. The open boundary was prescribed as a circle with a radius of 1 m to maintain geometric consistency between the two simulations. The water column was discretized into ten uniformly distributed sigma layers.

After a full tidal cycle (scaled as 4481 s) of rotational currents, the standalone FVCOM simulation produced a maximum scour depth of 0.2 S/D, which was approximately 15% shallower than the depth simulated by SedFoam (Figure 10(b)). At a radial distance of 3D from the monopile, SedFoam continued to show scour depths of 0.2 S/D, whereas FVCOM indicated only 0.05 S/D at the same distance.

The scour morphology also differed markedly between the two models. Under rotational flow conditions, SedFoam produced a circular scour pattern that was consistent with observations (Figure 9). In contrast, FVCOM produced an asymmetric pattern with scour concentrated primarily on the western side of the monopile. This asymmetry was attributed to an underestimation of upstream scour in FVCOM. As the flow direction rotated, the insufficient erosion could not maintain the development of the scour hole, resulting in sediment backfilling. Therefore, only the scour hole formed during the later stages of the west-to-east flow was retained in the FVCOM simulation.

FVCOM represents a typical GFD model and generally uses turbulence closures such as the Mellor–Yamada Level 2.5 scheme together with a relatively coarse vertical sigma-layer discretization. Although this configuration is suitable for simulating large-scale coastal circulation and stratification, it does not adequately resolve near-bed turbulent structures, vertical acceleration and boundary layer dynamics (Kim & Moon, 2020; Qu et al., 2016; Tang et al., 2014), which are critical to scour development. The above comparisons, therefore indicate that a coupled GFD–CFD framework is required to simulate monopile scour under realistic, time-varying hydrodynamics. By combining the large-scale tidal circulation provided by FVCOM with the high-resolution turbulence and sediment-transport processes resolved by SedFoam, the coupled approach offers a more reasonable representation of scour evolution.

4.4. Mass and momentum conservation

To verify that the nesting interface preserves the mass and momentum transferred from the regional model to the local model, a quantitative consistency check was performed at the common boundary. Because the coupling is one-way, only the time-varying velocity field is prescribed from FVCOM at the inflow boundary, whereas the outflow is allowed to adjust freely to accommodate the wake dynamics resolved by the CFD model (Pang et al., 2024). The check therefore focuses on the inflow portion of the interface. The inflow volume flux and the density-normalized momentum flux along the in-flow direction were evaluated as

$$Q_{\text{in}} = \int_{A_{\text{in}}} |u_n| \, dA, \tag{16}$$

$$M = \int_{A_{\text{in}}} |u_n| U \, dA, \tag{17}$$

where $u_n = \mathbf{u} \cdot \mathbf{n}$ is the normal velocity across the common boundary, A_{in} denotes the inflow part of the nesting

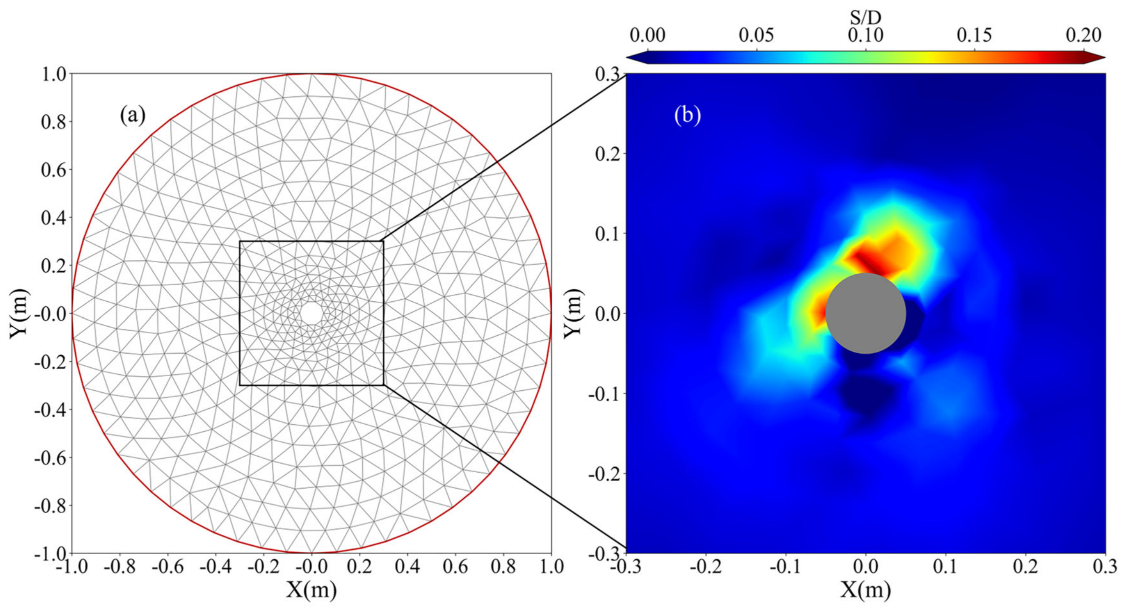

Figure 10. (a) FVCOM computational mesh is used for the scour simulation under rotating flow conditions. The red lines indicate the location of the open boundary. (b) Enlarged view of the simulated scour hole around the monopile after 4481 s, with the colorbar representing the normalized scour depth (S/D).

interface, and U is the velocity component along the incoming-flow direction. The absolute relative difference was calculated as

$$\varepsilon = \frac{|X_{\mathrm{OpenFOAM}} - X_{\mathrm{FVCOM}}|}{|X_{\mathrm{FVCOM}}|} \times 100\%, \qquad (18)$$

where Xrepresents either Q_{in} or M. The average absolute relative difference is 0.267% for the inflow volume flux and 1.222% for the momentum flux. These small differences, which are mainly induced by fifth-order interpolation in the vertical profiles, indicate that the mass and momentum input imposed at the SedFoam boundary is consistent with the FVCOM-derived boundary forcing, confirming that the nesting interface preserves the main inflow mass and momentum transfer from the regional GFD model to the local CFD model.

5. Practical application

5.1. Study area and scour observations

The coupled framework was subsequently applied to a real-world scenario at the Changyi offshore wind farm, situated in Laizhou Bay of the Bohai Sea, China (Figure 11(a)). This location is positioned 14–18 km offshore, with water depth ranging from 6 to 9 metres. By the end of 2023, the wind farm hosted 50 wind turbines, each with a rated capacity of 6 MW, resulting in a total installed capacity of 300 MW. All turbines are supported by monopile foundations.

The dominant hydrodynamic process in Laizhou Bay is the semi-diurnal astronomical tide. The average tidal range varies between 0.92 and 1.43 m, increasing progressively from north to south (You & Chen, 2019). Among the observed sediment samples, 52.5% are identified as sandy silt, followed by silt at 32.5%, mud at 12.5%, and silty sand at 2.5%. The median sediment size ranges from 16.54 µm to 109.14 µm, with a median size of 58.96 µm (Zhao et al., 2021).

In August 2023, field observations were conducted over a complete spring-neap tidal cycle to investigate hydrodynamic and morphological conditions around OWT foundations. A single-beam sonar measured detailed bathymetric data of the OWT foundations. Simultaneously, tide gauges recorded water level fluctuations. Additionally, an Acoustic Doppler Current Profiler (ADCP) was deployed to measure flow velocity, capturing variations in both current magnitude and direction throughout the observational period.

5.2. FVCOM configuration

An FVCOM unstructured mesh was used to spatially discretize the Changyi offshore wind farm, the neighbouring coastline, and Laizhou Bay areas (Figure 11(a)). The mesh effectively captured shoreline geometries with a resolution of 1 km, while the islands were resolved at 500 m. Following the methodology of Cazenave et al. (2016) and Pang et al. (2024), the resolution around the monopile foundations, which have a diameter of $\sim$10 metres, was refined to 2.5 metres (red curves in Figure 11(d)). At the lateral open boundary, the resolution gradually increased to 10 kilometres (Figure 11(a)).

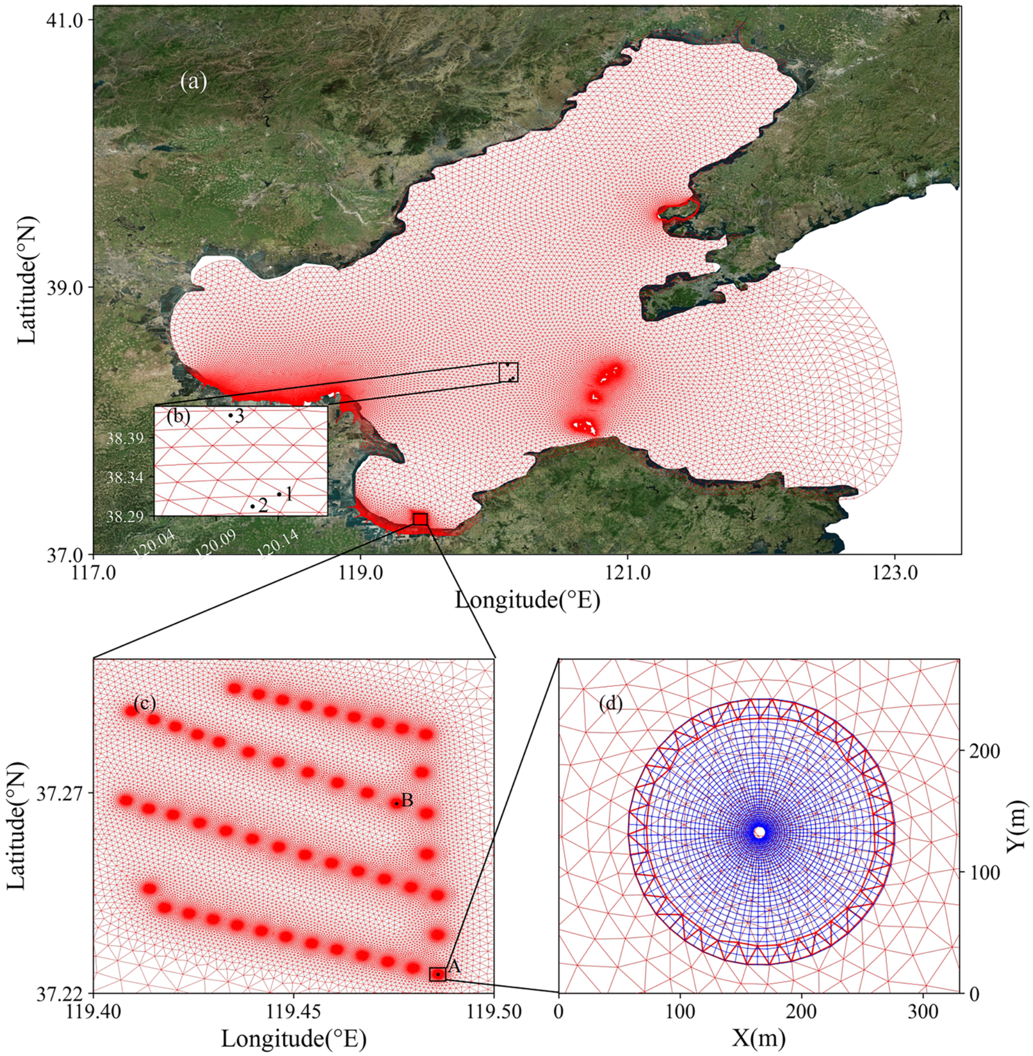

Figure 11. (a) Unstructured-grid mesh of FVCOM model for the Bohai Sea and adjacent regions; (b) locations of tide gauge stations and observation sites for validation; (c) the enlarged view of the Changyi offshore wind farm; and (d) one single wind turbine with an overlapping structured grid of OpenFOAM. The gauge station 1 is shown in panel (b) using black text, as well as the observation sites 2 and 3. The black dots in panel (c) indicate selected monopiles A and B. The red mesh in (d) represents the FVCOM mesh, the blue lines indicate the OpenFOAM grid, and the bold red mesh shows the nesting boundary.

Given the shallow local water depth, the water column was discretized into ten uniformly distributed sigma layers. Eight major astronomical tidal components were included in the open boundary conditions, comprising four diurnal constituents (K_1, O_1, P_1, and Q_1) and four semi-diurnal constituents (M_2, S_2, N2, and K_2), retrieved from the TPXO 8 dataset (Egbert & Erofeeva, 2002). Atmospheric forcing, including sea surface wind and precipitation, was sourced from the ERA5 dataset provided by the European Centre for Medium-Range Weather Forecasts (ECMWF), with a spatial resolution of 0.25° and a temporal resolution of 3 h. Temperature and salinity fields were initialized using data from the Global Ocean Forecasting System (GOFS) version 3.1, derived from the GLBy0.08 grid of the global Hybrid Coordinate Ocean Model (HYCOM) (Bleck, 2002). This dataset also provided salinity, temperature, and volume transport along the lateral boundary. To ensure computational stability and accuracy, the simulation employed external and internal time steps of 0.5 and 2.5 s, respectively.

5.3. FVCOM validation

To assess model performance and reliability, the model was validated using tide and flow conditions in May 2012. Tidal gauge data from the Bohai Sea were employed to validate the FVCOM simulated tides (Figure 11(b)). The results indicate that FVCOM accurately captured the tidal patterns in the Bohai Sea and Laizhou Bay area (Figure 12), with a root mean square error (RMSE) of 0.09 m.

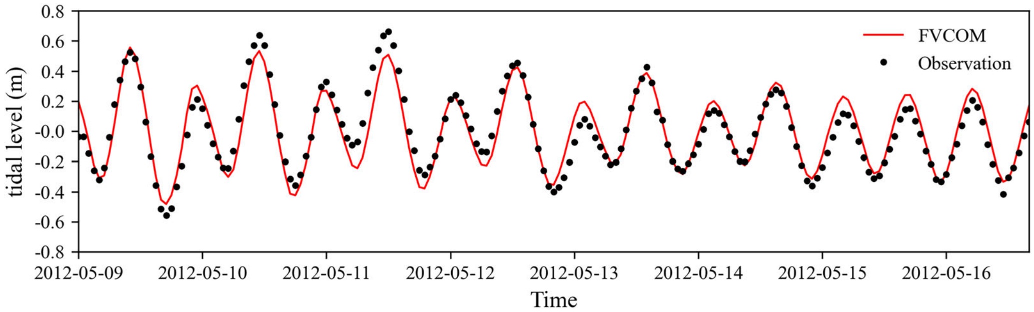

Figure 12. Comparison between observed (black dot) and FVCOM simulated (red line) tide elevation at the gauge station.

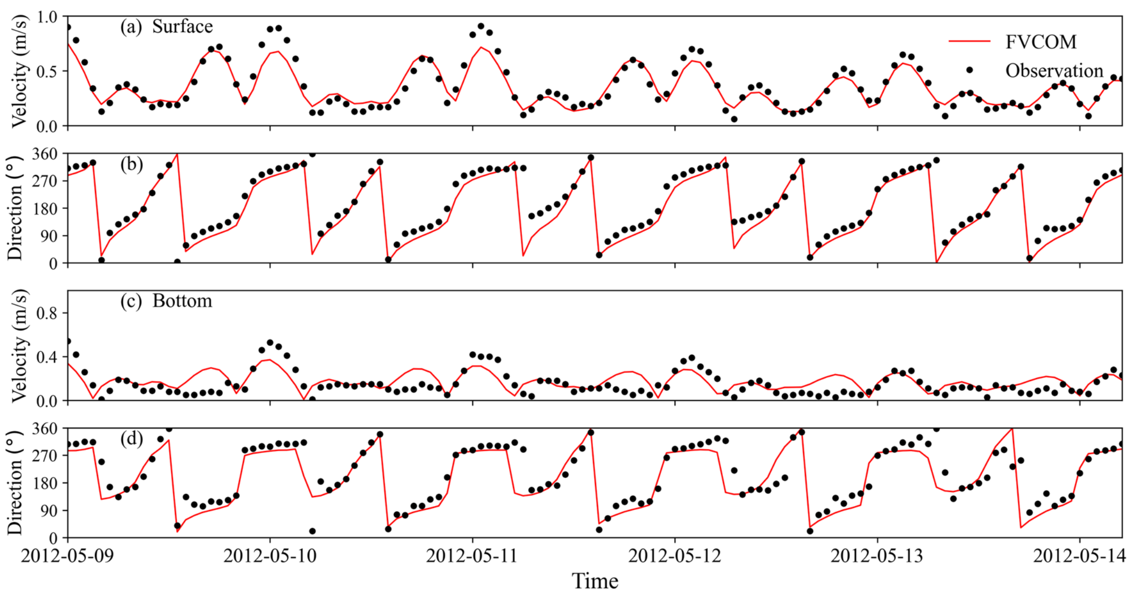

Figure 13. Model-data comparison at station 2 (in Figure 11) between observed (black dots) and simulated (red lines) surface velocity (a), surface direction (b), bottom velocity (c), and bottom direction (d), respectively.

The simulated flow patterns were validated against observed surface and bottom velocity and direction data from two measurement sites located in the Bohai Sea (Figure 11(b)). The simulation results at Station 2 showed RMSE values of 0.08 and 0.09 m/s for surface and bottom velocities, 25.50° and 47.26° for surface and bottom directions, respectively (Figure 13). The model-data comparison at Station 3, had RMSE values of 0.06 and 0.09 m/s for surface and bottom velocities, 23.97° and 35.71° for surface and bottom directions, respectively (Figure 14). The model results demonstrated strong agreement with the observed data, particularly in the surface layer, where FVCOM effectively captured the tidal flow variation in both flow velocity and direction (Figures 13 and 14(a,b)). In the bottom layer, the model slightly overestimated flow velocity during slack water periods, leading to higher errors compared to the surface layer (Figure 13c-d and Figure 14c-d). Since the flow velocities were much lower ($<$ 0.1 m/s) during these periods, it was relatively difficult for numerical simulations to capture such low velocities. In general, FVCOM successfully reproduced the key hydrodynamic characteristics of the Bohai Sea and Laizhou Bay region. The analysis of surface and bottom currents confirms that the central region of Bohai Bay is influenced by rotating currents, with periodic variations in flow direction.

5.4. OpenFOAM setup and coupling

Following the nesting boundary method, a unified OpenFOAM model mesh was configured (Figure 15). Given the limited extent of monopile scour holes, the outer nesting boundary radius was set to 100 metres based on previous studies, indicating that scour holes typically extended 3–5 S/D (Askarinejad et al., 2022; Wang et al., 2020). The model resolution was configured as 0.25 metres around the monopile foundation and 3 metres along the nesting boundary (Figure 15(a)). A specific OWT (monopile A in Figure 11) located at 119.4861°E, 37.2247°N was selected for the coupling simulation, with

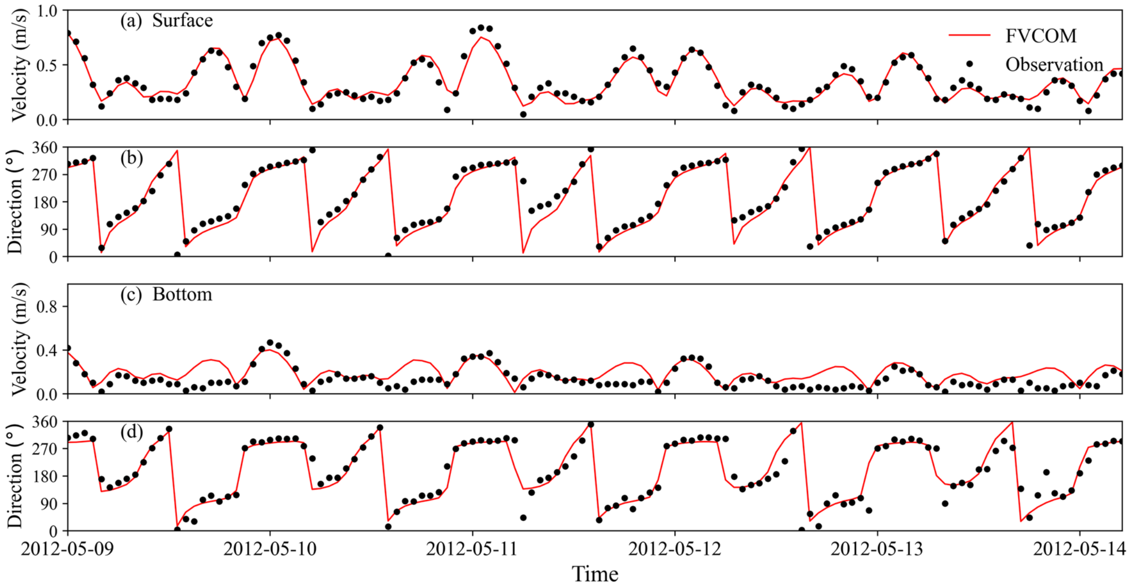

Figure 14. Model-data comparison at station 3 (in Figure 11) between observed (black dots) and simulated (red lines) surface velocity (a), surface direction (b), bottom velocity (c), and bottom direction (d), respectively.

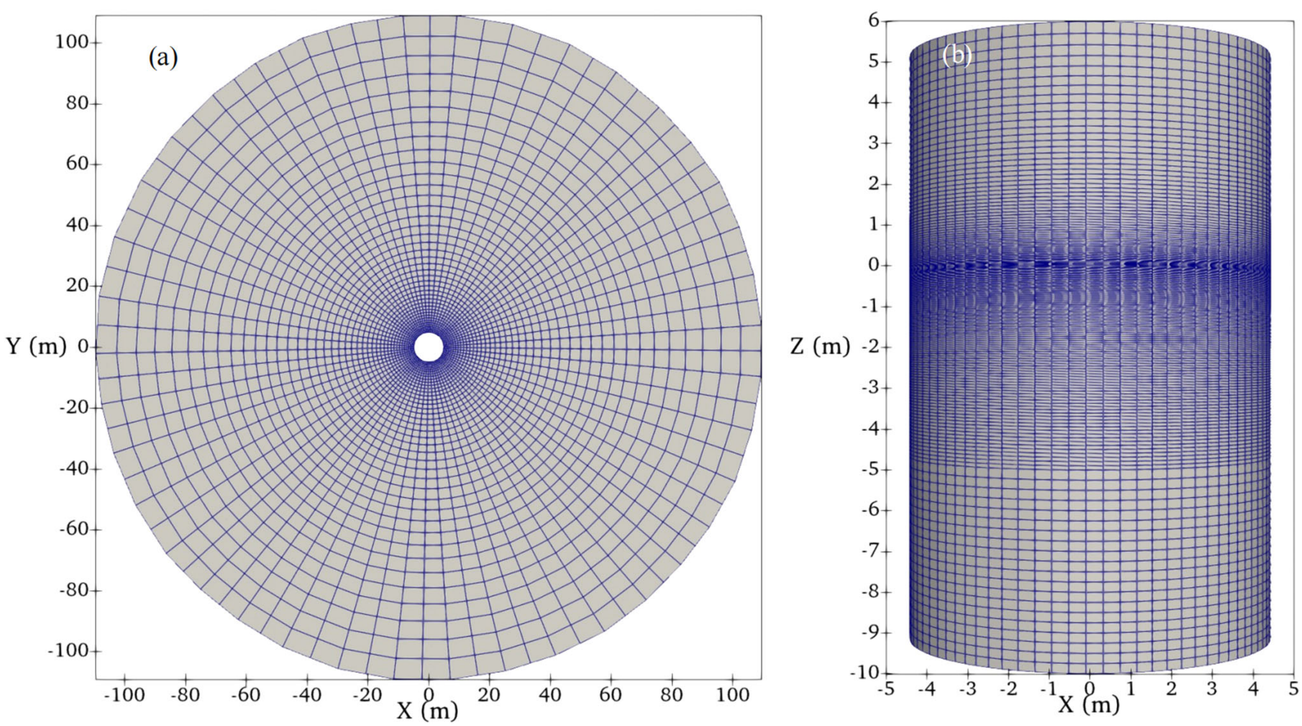

Figure 15. Model grids in the horizontal (a) and vertical (b) direction of the selected Changyi OWT.

a water depth of approximately 6 metres. The water column was discretized into 96 layers, ensuring a higher resolution of 0.02 metres near the water bottom and 0.3 metres near the sea surface (Figure 15(b)). The maximum time step was set to 0.03 s. Boundary conditions were established using second-order temporal interpolation from FVCOM modelling results, including the vertical flow profile, as described in Pang et al. (2024). The initial bottom bathymetry in the local CFD domain was set as a uniformly flat seabed based on the local water depth around the selected monopile. The CFD model underwent a one-hour ramp time period, transitioning from zero initialization to steady-state flow. Subsequently, the FVCOM-OpenFOAM coupled modelling framework ran for two tidal cycles during spring tide period on August 5, 2023.

It should be noted that the present simulation was designed as an event-scale demonstration under

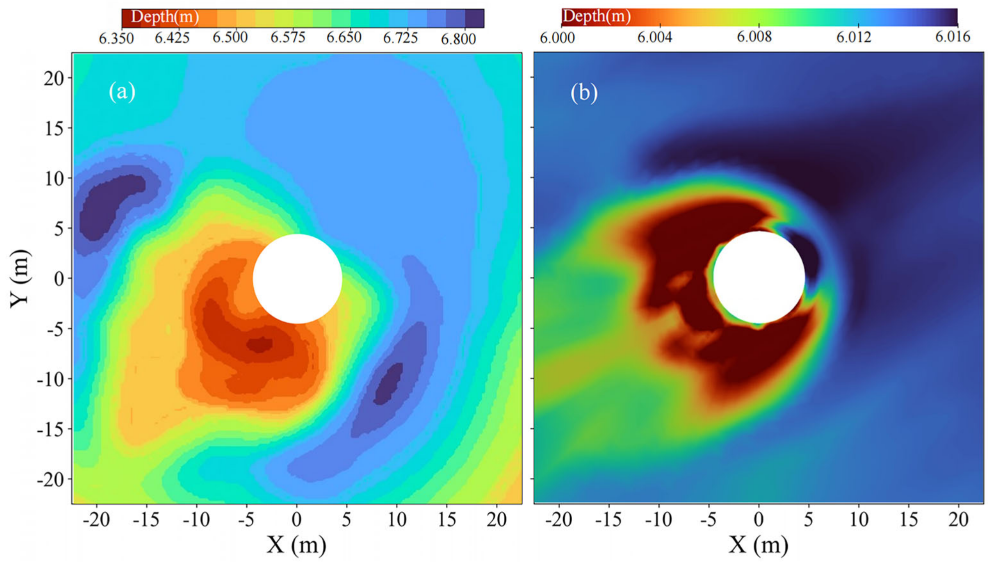

Figure 16. Depth around the monopile A measured by the single-beam echo sounder (a), and simulated by the coupled modelling framework (b).

energetic spring-tide forcing rather than as an estimate of equilibrium scour. Monopile scour is known to evolve toward equilibrium over timescales longer than a few tidal cycles (Johnson & McCuen, 1991; Melville & Chiew, 1999; Wang, 2015). The two-cycle duration provides an event-scale assessment of the initial morphodynamic response of the seabed to realistic, time-varying tidal forcing. The analysis focuses on the spatial distribution of erosion and deposition, the preferential scour region. It helps identify erosion-prone areas around the foundation and supports monitoring design and preliminary evaluation of scour protection requirements.

5.5. Scouring results

Single-beam sonar scanning captured the actual scour patterns and depths induced by tidal currents. The observed results revealed that backfilling around the monopile predominantly in the southwest direction (Figure 16(a)). In the actual scour patterns, the deepest scour depths were observed in the northwest and southeast directions, corresponding to the monopile's lateral sides. Notably, scour depth and extent were more pronounced in the northwest direction compared to the southeast direction.

The scour simulation results are shown in Figure 16b. After two tidal cycles, the interaction between currents and sediments around the monopile foundation exhibited a highly intricate and dynamic response. Simulated scour was primarily observed in the northwest part around the monopile, with the most significant scour occurring in the north part of the monopile. This aligns with the observed pattern, i.e. the scour distributed in the relatively northwest area of the monopile and was more significant in the north. The simulated scour depth reached up to 6.01 metres, consistent with the observed values (6.80 m) in magnitude. In simulated results, significant deposition was also observed on the southwest side, highly aligning with the observed data in the deposition pattern.

Due to the limited duration of two tidal cycles, conclusions on equilibrium depth or long-term scour rate were not supported by this simulation. Furthermore, since the field dataset consists of a post-event bathymetric snapshot without time-resolved evolution, Figure 16 was used to evaluate agreement in spatial scour/deposition pattern and scour magnitude, rather than to directly validate scour dynamics. The results were restricted to the corresponding short-term response. Under these constraints, agreement was obtained in the dominant areas of scour and deposition around the monopile.

6. Discussions

6.1. Scour at different monopiles: impact of tidal currents

To investigate the mechanism of the observed scour at selected monopile A, spring-tide currents in July 2023 were examined using FVCOM (Figure 17(a)). Hourly-averaged tidal currents exhibited a predominantly reciprocating pattern along a northeast–southwest axis, consistent with previous studies for Laizhou Bay (Sun et al., 2024; Wang et al., 2009). The maximum hourly-averaged

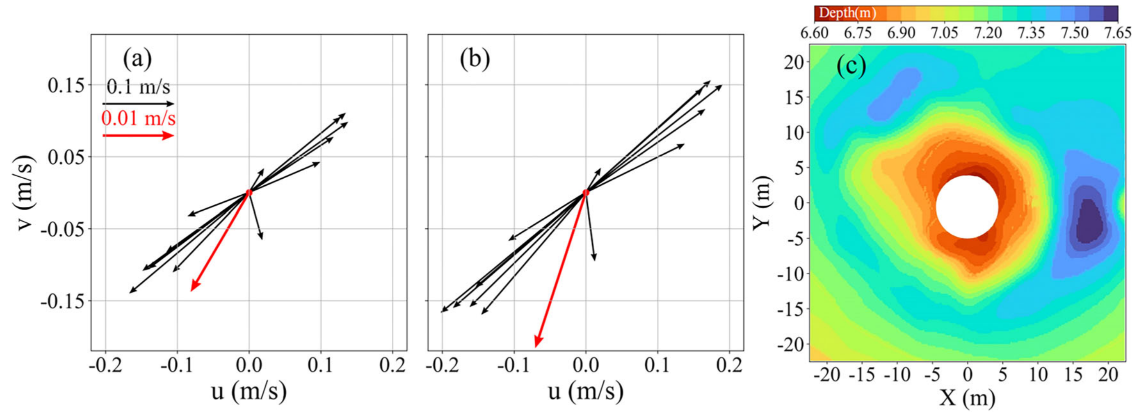

Figure 17. Hourly tidal currents (black arrows) and the residual flow (red arrow) at monopile A (a) and monopile B (b) during a spring tide cycle; (c) depth around the monopile B measured by the single-beam echo sounder, corresponding to Figure 16a.

velocity during the flood tide reached 0.22 m/s, compared with 0.17 m/s during ebb tide, indicating that the flood tide was dominant driving force. The monthly mean residual current direction, obtained by low-pass filtering to remove periodic tidal variations, was also oriented from northeast to southwest with a direction of approximately 240° (red arrow in Figure 17(a)), in agreement with earlier numerical results (Chi et al., 2020). A similar pattern of tidal currents was detected at monopile B (Figure 17(b)), located farther offshore near the wind farm centre (Figure 11(c)). The maximum hourly-averaged velocities during flood and ebb tides at monopile B were 0.26 and 0.24 m/s, respectively. The monthly mean residual current direction at monopile B also aligned with the northeast–southwest axis. The consistent flood-dominant forcing at monopiles A and B is reflected in the similar scour response (Figures 16a and 17c). Both monopiles presented backfilling along the northeast and southwest directions, while scouring concentrated on the lateral sides, forming a near-symmetric scour pattern aligned with the dominant tidal axis.

The circulation characteristics were further examined at monopiles A and B using a climatological FVCOM simulation. To present typical wind forcing, 10 m height wind fields from the ECMWF ERA5 hourly reanalysis dataset (1994–2023) were averaged. The data were regridded to a regular 0.25° × 0.25° latitude–longitude grid, ensuring spatial consistency across the simulation domain. All other model configurations remained consistent with previous simulations. The simulated summer flow fields were then averaged to represent the typical summer residual circulation in Laizhou Bay (Figure 18(a)). At monopile A, the residual flow was directed predominantly from northeast to southwest (251°), broadly aligned with the local tidal axis (Figure 18(b)). In contrast, the residual circulation at monopile B was oriented from northwest to southeast, i.e. opposite to the local tidal axis.

Despite these differences in residual circulation, the observed scour patterns at monopiles A and B were both oriented along the tidal axis rather than the residual circulation direction. This consistency indicates that, for the conditions examined here, the tidal-current direction provides the primary directional control on the spatial pattern of scour and deposition features in the study area. It is therefore inferred that neglecting the tidal forcing can bias the predicted scour orientation.

The capability of the GFD–CFD framework to reproduce the observed scour pattern highlights the importance of incorporating realistic, time-varying hydrodynamic forcing in monopile scour simulations. In many coastal and offshore environments, the tidal currents can depart from idealized unidirectional or bidirectional simplifications due to bathymetric complexity, wind effects, or residual circulation. Therefore, relying solely on simplified flow assumptions can lead to inaccurate predictions. The present framework provides a practical route to couple large-scale tidal variability resolved by a GFD model with near-bed turbulence and sediment processes resolved by CFD, and is therefore potentially applicable to a wider range of hydrodynamic conditions beyond the reciprocal tide considered here.

6.2. Limitations and future prospects

Although the comparison between model results and measurements demonstrates good agreement in the morphological characteristics of the scour holes, the limited simulation duration remains a constraint. The present modelling framework is limited to a few tidal cycles due to the high computational demand of CFD simulations. However, coastal dynamics span multiple temporal scales, from tidal cycles to seasonal and interannual

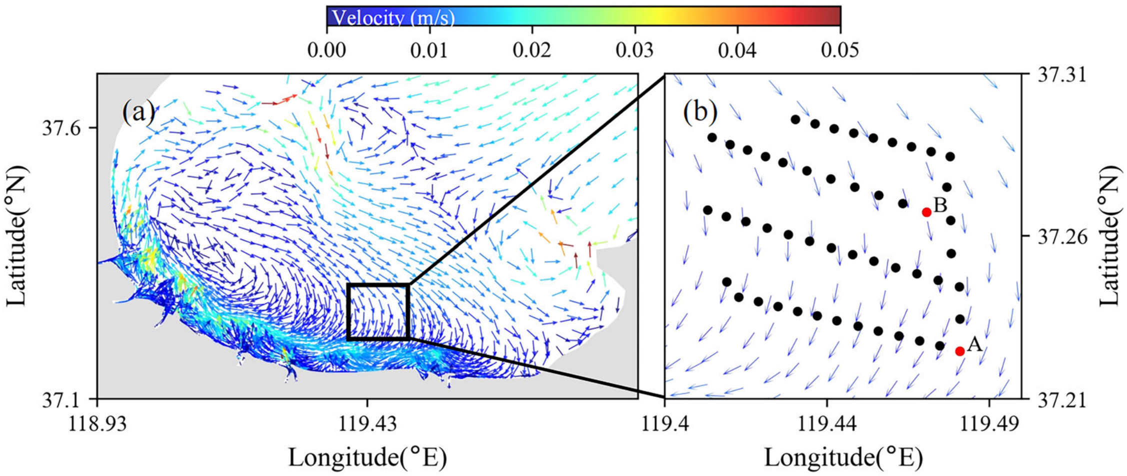

Figure 18. Climatological circulations in the Laizhou Bay in summer (a) and an enlarged view of the Changyi offshore wind farm (b). The black dots in (b) represent OWT locations, and the red dots indicate selected monopiles A and B.

changes. Additionally, these OWT are expected to operate for decades. Under such constraints, simulations over one to two tidal cycles should be interpreted as event-scale responses rather than long-term evolution. A common strategy to extend morphodynamic simulations is the use of a morphological acceleration factor, in which a scalar multiplier is applied to the sediment-continuity (Exner) equation to accelerate bed-level change (Lesser et al., 2004; Morgan et al., 2020). Acceleration ratios typically ranging from 10 to 1000 and have been widely used for riverine and estuarine morphological evolution (Jones et al., 2007; Li et al., 2018; Morgan et al., 2020; Van der Wegen & Roelvink, 2008). In future development, this strategy will be incorporated into the SedFoam component of the coupled framework by introducing an acceleration factor into the sediment-continuity equation. The hydrodynamic field will be solved at the physical time scale, while the sediment response to the computed flow forcing will be accelerated through the modified sediment-continuity equation. This treatment is expected to reduce the computational cost of long-duration scour simulations while retaining the resolved near-pile flow structures and tidal forcing, thereby improving the applicability of the coupled framework to longer-term morphological prediction.

Additionally, extreme events are not yet represented. Storms and the associated wave-current interaction can intensify flow velocity and pressure around OWT structures, increasing sediment transport capacity and potentially enhancing scour (Galano et al., 2021; Whitehouse et al., 2011; Yao et al., 2024). Extending the framework to include wave effects will allow the sensitivity of scour to episodic high-energy forcing to be assessed, which is particularly relevant given the projected changes in coastal extremes under climate change. A new numerical solver SedInterFoam, recently developed by the SedFoam team (Mathieu et al., 2025), provides a possible route for incorporating wave effects into a physics-based sediment-transport model. It introduces an additional air phase, resolving the air–water interface using the volume-of-fluid method, and coupling with waves2Foam for wave generation and absorption. In future work, FVCOM could be coupled with the Simulating WAves Nearshore (SWAN) at the regional scale to provide realistic tidal-current and wave parameters (Chen et al., 2018), then nested into a local SedInterFoam domain to resolve wave–current–sediment interactions and its induced monopile scour evolution.

Finally, deposition and backfilling processes are only partially represented because the present setup focuses on single-fraction sediment transport and does not explicitly account for mixed sediments. Future work will consider multi-class sediment formulations and data-driven parameterization (e.g. machine-learning-assisted calibration) to constrain transport parameters using laboratory and field observations.

7. Conclusions

The main contribution of this study is the extension of GFD–CFD coupling from hydrodynamic simulation to sediment transport and scour morphodynamics by integrating FVCOM with SedFoam. FVCOM provides realistic time-varying regional tidal forcing, while SedFoam resolves scour evolution around monopile foundations. The framework is evaluated against two flume experiments under bidirectional forcing. The simulated scour evolution captured the main phases of scour development (initiation, growth and approach to equilibrium).

Across the laboratory cases, the RMSE of the normalized scour depth remained below 0.1 S/D, indicating that the coupled approach can represent not only final scour patterns but also the dynamic scour process over tidal cycles. Additionally, in an idealized experiment this framework successfully reproduces circular scour holes under rotating flow conditions. The framework is further applied to an actual OWF in Laizhou Bay, China, demonstrating good agreement between simulated and measured scour and backfilling patterns. For the two investigated monopiles, the similarity in scour planform between locations was aligned with a consistent dominant tidal axis, despite the differences of the residual circulation. These results suggest that tidal forcing provides the primary control on scour direction around the studied monopiles, highlighting the importance of incorporating actual tidal currents in simulating scour around offshore infrastructure. This study demonstrates the capability and practical relevance of the proposed modelling framework for resolving complex flow-sediment interaction and monopile scour under realistic offshore engineering conditions.

Author contributions

CRediT: **Jialin Pang:** Investigation, Methodology, Visualization, Writing – original draft; **Zaiyang Zhou:** Conceptualization, Funding acquisition, Methodology, Supervision, Writing – review & editing; **Xiaodao Wei:** Data curation; **Jianzhong Ge:** Conceptualization, Funding acquisition, Supervision, Writing – review & editing

Disclosure statement

No potential conflict of interest was reported by the author(s).

Funding

This research is supported by the National Natural Science Foundation of China (Grant No. 42476160, 42406161), and the Research Project of China Three Gorges Corporation (Grant No. 202103552).

Code and data availability

Data are publicly available at https://doi.org/10.6084/m9.figshare.31979877.

References

Ahmad, N., Bihs, H., Kamath, A., & Arntsen, ØA. (2015). Three-dimensional cfd modeling of wave scour around side-by-side and triangular arrangement of piles with reef3d. *Procedia Engineering*, *116*, 683–690. https://doi.org/10.1016/j.proeng.2015.08.355

Ahmad, N., Bihs, H., Myrhaug, D., Kamath, A., & Arntsen, ØA. (2018). Three-dimensional numerical modelling of wave-induced scour around piles in a side-by-side arrangement. *Coastal Engineering*, *138*, 132–151. https://doi.org/10.1016/j.coastaleng.2018.04.016

Allen, B., & Kudrolli, A. (2018). Granular bed consolidation, creep, and armoring under subcritical fluid flow. *Physical Review Fluids*, *3*(7), 074305. https://doi.org/10.1103/PhysRevFluids.3.074305

Alvir, M., Grbčić, L., Sikirica, A., & Kranjčević, L. (2022). Openfoam-roms nested model for coastal flow and outfall assessment. *Ocean Engineering*, *264*, 112535. https://doi.org/10.1016/j.oceaneng.2022.112535

Askarinejad, A., Wang, H., Chortis, G., & Gavin, K. (2022). Influence of scour protection layers on the lateral response of monopile in dense sand. *Ocean Engineering*, *244*, 110377. https://doi.org/10.1016/j.oceaneng.2021.110377

Barrie, A., Wang, C., Liang, F., & Qi, W. (2024). Experimental investigation on the mechanism of local scour around a cylindrical coastal pile foundation considering sloping bed conditions. *Ocean Engineering*, *312*, 119225. https://doi.org/10.1016/j.oceaneng.2024.119225

Bleck, R. (2002). An oceanic general circulation model framed in hybrid isopycnic-cartesian coordinates. *Ocean modelling*, *4*(1), 55–88. https://doi.org/10.1016/S1463-5003(01)00012-9

Cazenave, P. W., Torres, R., & Allen, J. I. (2016). Unstructured grid modelling of offshore wind farm impacts on seasonally stratified shelf seas. *Progress in oceanography*, *145*, 25–41. https://doi.org/10.1016/j.pocean.2016.04.004

Chang, J., Lee, G. H., Harris, C. K., Figueroa, S. M., & Jung, N. W. (2023). Relative contribution of the presence of an estuarine dam and land reclamation to sediment dynamics of the Nakdong estuary. *Frontiers in Marine Science*, *10*, 1101658. https://doi.org/10.3389/fmars.2023.1101658

Chang, W. Y., & Constantinescu, G. (2023). Oscillatory flow around a vertical circular cylinder placed in an open channel: coherent structures, sediment entrainment potential and drag forces. *Journal of Fluid Mechanics*, *964*, A22. https://doi.org/10.1017/jfm.2023.367

Chauchat, J., Cheng, Z., Nagel, T., Bonamy, C., & Hsu, T. J. (2017). Sedfoam-2.0: A 3-d two-phase flow numerical model for sediment transport. *Geoscientific Model Development*, *10*(12), 4367–4392. https://doi.org/10.5194/gmd-10-4367-2017

Chen, C., Liu, H., & Beardsley, R. C. (2003). An unstructured grid, finite-volume, three-dimensional, primitive equations ocean model: Application to coastal ocean and estuaries. *Journal of Atmospheric and Oceanic Technology*, *20*(1), 159–186. https://doi.org/10.1175/1520-0426(2003)020<0159:AUGFVT>2.0.CO;2

Chen, T., Zhang, Q., Wu, Y., Ji, C., Yang, J., & Liu, G. (2018). Development of a wave-current model through coupling of fvcom and swan. *Ocean Engineering*, *164*, 443–454. https://doi.org/10.1016/j.oceaneng.2018.06.062

Cheng, Z., Hsu, T. J., & Chauchat, J. (2018). An Eulerian two-phase model for steady sheet flow using large-eddy simulation methodology. *Advances in Water Resources*, *111*, 205–223. https://doi.org/10.1016/j.advwatres.2017.11.016

Chernetsky, A. S., Schuttelaars, H. M., & Talke, S. A. (2010). The effect of tidal asymmetry and temporal settling lag on sediment trapping in tidal estuaries. *Ocean Dynamics*, *60*(5), 1219–1241. https://doi.org/10.1007/s10236-010-0329-8

Chi, W., Zhang, X., Zhang, W., Bao, X., Liu, Y., Xiong, C., Liu, J., & Zhang, Y. (2020). Impact of tidally induced residual circulations on chemical oxygen demand (COD) distribution in Laizhou Bay, China. *Marine Pollution Bulletin*, *151*, 110811. https://doi.org/10.1016/j.marpolbul.2019.110811

Clark, A. H., Shattuck, M. D., Ouellette, N. T., & O'Hern, C. S. (2015). Onset and cessation of motion in hydrodynamically sheared granular beds. *Physical Review E*, *92*(4), 042202. https://doi.org/10.1103/PhysRevE.92.042202

Dai, S., Han, B., Wang, B., Luo, J., & He, B. (2021). Influence of soil scour on lateral behavior of large-diameter offshore wind-turbine monopile and corresponding scour monitoring method. *Ocean Engineering*, *239*, 109809. https://doi.org/10.1016/j.oceaneng.2021.109809

Egbert, G. D., & Erofeeva, S. Y. (2002). Efficient inverse modeling of barotropic ocean tides. *Journal of Atmospheric and Oceanic Technology*, *19*(2), 183–204. https://doi.org/10.1175/1520-0426(2002)019<0183:EIMOBO>2.0.CO;2

Fredsøe, J., & Sumer, B. M. (2002). *The mechanics of scour in the marine environment.* Vol. 17. World Scientific Publishing Company .

Friedrichs, C. T., & Aubrey, D. G. (1988). Non-linear tidal distortion in shallow well-mixed estuaries: A synthesis. *Estuarine, Coastal and Shelf Science*, *27*(5), 521–545. https://doi.org/10.1016/0272-7714(88)90082-0

Galano, N., Moreno-Casas, P. A., & Abell, J. A. (2021). Extending the particle finite element method for sediment transport simulation. *Computer Methods in Applied Mechanics and Engineering*, *380*, 113772. https://doi.org/10.1016/j.cma.2021.113772

Geng, F., Yang, W., Nadimi, S., & Hu, Z. (2024). Development and prediction of scour around offshore wind turbine monopile foundations in ebb and flow tides. *Ocean Engineering*, *311*, 118905. https://doi.org/10.1016/j.oceaneng.2024.118905

Guan, D. W., Xie, Y. X., Yao, Z. S., Chiew, Y. M., Zhang, J. S., & Zheng, J. H. (2022). Local scour at offshore windfarm monopile foundations: A review. *Water Science and Engineering*, *15*(1), 29–39. https://doi.org/10.1016/j.wse.2021.12.006

Guo, X., Liu, J., Yi, P., Feng, X., & Han, C. (2022). Effects of local scour on failure envelopes of offshore monopiles and caissons. *Applied Ocean Research*, *118*, 103007. https://doi.org/10.1016/j.apor.2021.103007

Herdiansyah, S., Natakusumah, D. K., & Harlan, D. (2019). Fvcom model simulation of local scouring around bridge pile. In: MATEC Web of Conferences, EDP Sciences. p. 04020.

Hou, G., Xu, K., & Lian, J. (2022). A review on recent risk assessment methodologies of offshore wind turbine foundations. *Ocean Engineering*, *264*, 112469. https://doi.org/10.1016/j.oceaneng.2022.112469

Hu, W., Li, Y., Fan, Y., Xiong, M., Luo, H., McSaveney, M., Zheng, Y., & Tang, M. (2022). Flow amplification from cascading landslide dam failures: Insights from flume experiments. *Engineering Geology*, *297*, 106483. https://doi.org/10.1016/j.enggeo.2021.106483

Huang, W., Yang, Q., & Xiao, H. (2009). Cfd modeling of scale effects on turbulence flow and scour around bridge piers. *Computers & Fluids*, *38*(5), 1050–1058. https://doi.org/10.1016/j.compfluid.2008.01.029

Jia, W., & Yi, Y. (2023). Numerical study of the water-sediment regulation scheme (WSRS) impact on suspended sediment transport in the Yellow River estuary. *Frontiers in Marine Science*, *10*, 1135118. https://doi.org/10.3389/fmars.2023.1135118

Jindal, S., Rahmanli, U., Aleem, M., Cui, L., & Bhattacharya, S. (2024). Geotechnical challenges in monopile foundations and performance assessment of current design methodologies. *Ocean Engineering*, *310*, 118469. https://doi.org/10.1016/j.oceaneng.2024.118469

Johnson, P. A., & McCuen, R. H. (1991). A temporal, spatial pier scour model. 1319.

Jones, O., Petersen, O., & Kofoed-Hansen, H. (2007). Modelling of complex coastal environments: Some considerations for best practise. *Coastal Engineering*, *54*(10), 717–733. https://doi.org/10.1016/j.coastaleng.2007.02.004

Kazhyken, K., Videman, J., & Dawson, C. (2021). Discontinuous galerkin methods for a dispersive wave hydro-sediment-morphodynamic model. *Computer Methods in Applied Mechanics and Engineering*, *377*, 113684. https://doi.org/10.1016/j.cma.2021.113684

Kim, T., & Moon, J. H. (2020). Impact of improved mellor–yamada turbulence model on tropical cyclone-induced vertical mixing in the oceanic boundary layer. *Journal of Marine Science and Engineering*, *8*(7), 497. https://doi.org/10.3390/jmse8070497

Kopte, R., Becker, M., Holtermann, P., & Winter, C. (2022). Tides, stratification, and counter rotation: The German Bight rofi in comparison to other regions of freshwater influence. *Journal of Geophysical Research: Oceans*, *127*(6), e2021JC018236. https://doi.org/10.1029/2021JC018236

Lamb, M. P., Finnegan, N. J., Scheingross, J. S., & Sklar, L. S. (2015). New insights into the mechanics of fluvial bedrock erosion through flume experiments and theory. *Geomorphology*, *244*, 33–55. https://doi.org/10.1016/j.geomorph.2015.03.003

Lemasson, A. J., Somerfield, P. J., Schratzberger, M., Thompson, M. S. A., Firth, L. B., Couce, E., McNeill, C. L., Nunes, J., Pascoe, C., Watson, S. C. L., & Knights, A.M. (2024). A global meta-analysis of ecological effects from offshore marine artificial structures. *Nature Sustainability*, *7*(4), 485–495. https://doi.org/10.1038/s41893-024-01311-z

Lesser, G. R., Roelvink, J. v., van Kester, J. T. M., & Stelling, G. (2004). Development and validation of a three-dimensional morphological model. *Coastal Engineering*, *51*(8-9), 883–915. https://doi.org/10.1016/j.coastaleng.2004.07.014

Li, L., Shen, F., He, Z., Ma, G., Wang, J., & Huangfu, K. (2024). Contribution of high turbidity to tidal dynamics in a curved channel in Zhoushan Islands, China. *Engineering Applications of Computational Fluid Mechanics*, *18*(1), 2345161. https://doi.org/10.1080/19942060.2024.2345161

Li, L., Storms, J., & Walstra, D. (2018). On the upscaling of process-based models in deltaic applications. *Geomorphology*, *304*, 201–213. https://doi.org/10.1016/j.geomorph.2017.10.015

Lu, H., Wang, X., Bai, Z., Jia, N., & Xia, H. (2024). FVCOM-CFD model-based study of hydraulic turbine arrays in Mount Putuo tidal current energy test site. *Ocean Engineering*, *312*, 119079. https://doi.org/10.1016/j.oceaneng.2024.119079

Margheritini, L., Frigaard, P., Martinelli, L., Lamberti, A., 2006. Scour around monopile foundations for off-shore wind turbines, In: The First International Conference on the Application of Physical Modelling to Port and Coastal Protection (CoastLab06), Faculty of Engineering, University of Porto.
Mathieu, A., Chauchat, J., Bonamy, C., & Nagel, T. (2019). Two-phase flow simulation of tunnel and lee-wake erosion of scour below a submarine pipeline. *Water*, *11*(8), 1727. https://doi.org/10.3390/w11081727
Mathieu, A., Kim, Y., Hsu, T. J., Bonamy, C., & Chauchat, J. (2025). sedinterfoam 1.0: A three-phase numerical model for sediment transport applications with free surfaces. *Geoscientific Model Development*, *18*(5), 1561–1573. https://doi.org/10.5194/gmd-18-1561-2025
Mellor, G. L., & Yamada, T. (1982). Development of a turbulence closure model for geophysical fluid problems. *Reviews of Geophysics*, *20*(4), 851–875. https://doi.org/10.1029/RG020i004p00851
Melville, B. W., & Chiew, Y. M. (1999). Time scale for local scour at bridge piers. *Journal of Hydraulic Engineering*, *125*(1), 59–65. https://doi.org/10.1061/(ASCE)0733-9429(1999)125:1(59)
Morgan, J. A., Kumar, N., Horner-Devine, A. R., Ahrendt, S., Istanbulluoglu, E., & Bandaragoda, C. (2020). The use of a morphological acceleration factor in the simulation of large-scale fluvial morphodynamics. *Geomorphology*, *356*, 107088. https://doi.org/10.1016/j.geomorph.2020.107088
Nagel, T., Chauchat, J., Bonamy, C., Liu, X., Cheng, Z., & Hsu, T. J. (2020). Three-dimensional scour simulations with a two-phase flow model. *Advances in Water Resources*, *138*, 103544. https://doi.org/10.1016/j.advwatres.2020.103544
Niedoroda, A., & Dalton, C. (1982). A review of the fluid mechanics of ocean scour. *Ocean Engineering*, *9*(2), 159–170. https://doi.org/10.1016/0029-8018(82)90011-7
O'Kelly, B., & Arshad, M. (2016). Offshore wind turbine foundations: analysis and design. In Ng, C., Ran, L. (Eds.), *Offshore wind farms: Technologies, design and operation*. (pp. 589–610). Woodhead Publishing.https://doi.org/10.1016/B978-0-08-100779-2.00020-9
Pang, J., Ge, J., Tao, Y., Zhou, Q., & Zhou, Z. (2024). Simulating cross-scale flow dynamics around offshore monopile foundations with a gfd-cfd coupled model. *Ocean Engineering*, *312*, 119200. https://doi.org/10.1016/j.oceaneng.2024.119200
Paulsen, B. T., Bredmose, H., & Bingham, H. B. (2014). An efficient domain decomposition strategy for wave loads on surface piercing circular cylinders. *Coastal Engineering*, *86*, 57–76. https://doi.org/10.1016/j.coastaleng.2014.01.006
Pietrzak, J., Jakobson, J. B., Burchard, H., Vested, H. J., & Petersen, O. (2002). A three-dimensional hydrostatic model for coastal and ocean modelling using a generalised topography following co-ordinate system. *Ocean Modelling*, *4*(2), 173–205. https://doi.org/10.1016/S1463-5003(01)00016-6
Qi, J., Jing, Y., Chen, C., & Zhang, J. (2023). Numerical simulation of tidal current and sediment movement in the sea area near Weifang Port. *Water*, *15*(14), 2516. https://doi.org/10.3390/w15142516
Qin, B., Qu, R., Yang, W., & Xie, Y. (2024). A study on the scour surrounding the fixed foundation of an offshore wind turbine under complex waves, tidal currents, and pile vibration conditions. *Energies*, *17*(7), 1561. https://doi.org/10.3390/en17071561
Qu, K., Tang, H., & Agrawal, A. (2019). Integration of fully 3d fluid dynamics and geophysical fluid dynamics models for multiphysics coastal ocean flows: Simulation of local complex free-surface phenomena. *Ocean Modelling*, *135*, 14–30. https://doi.org/10.1016/j.ocemod.2019.01.001
Qu, K., Tang, H., Agrawal, A., Jiang, C., & Deng, B. (2016). Evaluation of sifom-fvcom system for high-fidelity simulation of small-scale coastal ocean flows. *Journal of Hydrodynamics*, *28*(6), 994–1002. https://doi.org/10.1016/S1001-6058(16)60701-1
Salimi-Tarazouj, A., Hsu, T. J., Traykovski, P., Cheng, Z., & Chauchat, J. (2021). A numerical study of onshore ripple migration using a Eulerian two-phase model. *Journal of Geophysical Research: Oceans*, *126*(2), e2020JC016773. https://doi.org/10.1029/2020JC016773
Schendel, A., Hildebrandt, A., Goseberg, N., & Schlurmann, T. (2018). Processes and evolution of scour around a monopile induced by tidal currents. *Coastal Engineering*, *139*, 65–84. https://doi.org/10.1016/j.coastaleng.2018.05.004
Shields, A. (1936). Anwendung der aehnlichkeitsmechanik und der turbulenzforschung auf die geschiebebewegung. *Mitteilungen der Preussischen Versuchsanstalt für Wasserbau und Schiffbau*, *26*, 5 .
Shi-Yang, Y., Xia, Y. Z., & Wang, S. H. (2021). Local scour around a monopile in reciprocating tidal current considering the effect of water depth. In: Journal of Physics: Conference Series, IOP Publishing. p. 012019.
Smagorinsky, J. (1963). General circulation experiments with the primitive equations: I. The basic experiment. *Monthly Weather Review*, *91*(3), 99–164. https://doi.org/10.1175/1520-0493(1963)091<0099:GCEWTP>2.3.CO;2
Solberg, T., Hjertager, B. H., & Bove, S. (2005). *CFD modelling of scour around offshore wind turbines in areas with strong currents. Technical Report*. Citeseer.
Sun, J., Peng, L., Zhu, X., Li, Z., Shi, H., Zhan, C., & You, Z. (2024). The effects of changes in the coastline and water depth on tidal prism and water exchange of the Laizhou Bay, China. *Frontiers in Marine Science*, *11*, 1459482. https://doi.org/10.3389/fmars.2024.1459482
Tang, H., Qu, K., & Wu, X. (2014). An overset grid method for integration of fully 3d fluid dynamics and geophysics fluid dynamics models to simulate multiphysics coastal ocean flows. *Journal of Computational Physics*, *273*, 548–571. https://doi.org/10.1016/j.jcp.2014.05.010
Van der Wegen, M., & Roelvink, J. (2008). Long-term morphodynamic evolution of a tidal embayment using a two-dimensional, process-based model. *Journal of Geophysical Research: Oceans*, *113*(C3), C03016. https://doi.org/10.1029/2006JC003983
Van Rijn, L. C. (1984). Sediment transport, Part I: Bed load transport. *Journal of Hydraulic Engineering*, *110*(10), 1431–1456. https://doi.org/10.1061/(ASCE)0733-9429(1984)110:10(1431)
Vindenes, H., Orvik, K. A., Søiland, H., & Wehde, H. (2018). Analysis of tidal currents in the North Sea from ship-board acoustic Doppler current profiler data. *Continental Shelf Research*, *162*, 1–12. https://doi.org/10.1016/j.csr.2018.04.001

Wang, C., Wu, Q., Liang, J., Liang, F., & Yu, X. B. (2024). Establishment and implementation of an artificial intelligent flume for investigating local scour around underwater foundations. *Transportation Geotechnics*, *49*, 101433. https://doi.org/10.1016/j.trgeo.2024.101433

Wang, J. (2015). Research on local scour at bridge pier under tidal action. In: MATEC Web of Conferences, EDP Sciences. p. 01013.

Wang, Q., Zhang, M., Zhong, S., Du, G., Jin, B., Yang, H., & Song, C. (2009). Dynamic sedimentation and geomorphologic evolution of the Laizhou shoal, Bohai Sea, Northern China. *Journal of Asian Earth Sciences*, *36*(2-3), 196–208. https://doi.org/10.1016/j.jseaes.2009.06.001

Wang, S. Y., Qi, W. G., Li, B., Wang, C., & Gao, F. P. (2024). Tidal currents-induced scour development around pile foundations: Effects of flow velocity hydrograph. *Coastal Engineering*, *191*, 104533. https://doi.org/10.1016/j.coastaleng.2024.104533

Wang, Z., Hu, R., Leng, H., Liu, H., Bai, Y., & Lu, W. (2020). Deformation analysis of large diameter monopiles of offshore wind turbines under scour. *Applied Sciences*, *10*(21), 7579. https://doi.org/10.3390/app10217579

Wang, Z., Wang, W., Qiu, W., & Jiang, M. (2024). Experimental study on wave-induced loads and nonlinear effects for pier-pile group foundations of sea-crossing bridges: Wave slamming and suction effect. *Coastal Engineering*, *192*, 104567. https://doi.org/10.1016/j.coastaleng.2024.104567

Weller, H. G., Tabor, G., Jasak, H., & Fureby, C. (1998). A tensorial approach to computational continuum mechanics using object-oriented techniques. *Computers in physics*, *12*(6), 620–631. https://doi.org/10.1063/1.168744

Whitehouse, R., Sutherland, J., & O'Brien, D. (2006). Seabed scour assessment for offshore windfarm.

Whitehouse, R. J., Harris, J. M., Sutherland, J., & Rees, J. (2011). The nature of scour development and scour protection at offshore windfarm foundations. *Marine Pollution Bulletin*, *62*(1), 73–88. https://doi.org/10.1016/j.marpolbul.2010.09.007

Wu, H., Yu, H., Fang, Y., Zhou, Q., Zhuo, F., & Kelly, R. M. (2021). Assessment of the tidal current energy resources and the hydrodynamic impacts of energy extraction at the Puhu channel in Zhoushan Archipelago, China. *Journal of Ocean University of China*, *20*(3), 478–488. https://doi.org/10.1007/s11802-021-4767-3

Wu, X. G., & Tang, H. S. (2010). Coupling of CFD model and FVCOM to predict small-scale coastal flows. *Journal of Hydrodynamics*, *22*(S1), 284–289. https://doi.org/10.1016/S1001-6058(09)60208-0

Xiang, Q., Wei, K., Qiu, F., Yao, C., & Li, Y. (2020). Experimental study of local scour around caissons under unidirectional and tidal currents. *Water*, *12*(3), 640. https://doi.org/10.3390/w12030640

Yao, Y., Rao, M., Yu, C., Wu, Z., Zhang, C., & Wu, T. (2024). Influence of local scour on the dynamic responses of OWTS under wind-wave loads. *Frontiers in Marine Science*, *11*, 1476071. https://doi.org/10.3389/fmars.2024.1476071

You, Z. J., & Chen, C. (2019). Coastal dynamics and sediment resuspension in Laizhou Bay. In X. H. Wang (Ed.), *Sediment dynamics of Chinese muddy coasts and estuaries: physics, biology and their interactions* (pp. 123–142). Academic Press.

Zhang, J., Wang, F., Guo, Y., Chen, H., & Zhang, Q. (2023). Nested numerical simulation of multi-scale flow characteristics around monopile foundation of offshore wind farm at Weihai coastal water, China. *Ocean Engineering*, *288*, 116171. https://doi.org/10.1016/j.oceaneng.2023.116171

Zhang, T., Tian, B., Sengupta, D., Zhang, L., & Si, Y. (2021). Global offshore wind turbine dataset. *Scientific Data*, *8*(1), 191. https://doi.org/10.1038/s41597-021-00982-z

Zhang, Z., Du, S., Guo, Y., Yang, Y., Zeng, J., Sui, T., Wei, R., & Li, Z. (2023). Field study of local scour around bridge foundations on silty seabed under irregular tidal flow. *Coastal Engineering*, *185*, 104382. https://doi.org/10.1016/j.coastaleng.2023.104382

Zhang, Z., Guo, Y., Yang, Y., Shi, B., & Wu, X. (2021). Scale model experiment on local scour around submarine pipelines under bidirectional tidal currents. *Journal of Marine Science and Engineering*, *9*(12), 1421. https://doi.org/10.3390/jmse9121421

Zhao, E., Mu, L., & Shi, B. (2018). Numerical study of the influence of tidal current on submarine pipeline based on the SIFOM–FVCOM Coupling Model. *Water*, *10*(12), 1814. https://doi.org/10.3390/w10121814

Zhao, M. (2022). A review on recent development of numerical modelling of local scour around hydraulic and marine structures. *Journal of Marine Science and Engineering*, *10*(8), 1139. https://doi.org/10.3390/jmse10081139

Zhao, Y., You, L., Ma, Y., Song, X., Su, B., He, J., Fu, P., Wang, Y., & Sun, S. (2021). *Preliminary analysis of the relationship between sediment grain size and Macrobenthos community in Laizhou Bay [in Chinese]*. MARINE SCIENCE BULLETIN.

Zhou, J., Sun, B., Zhang, H., Yuan, S., & Tang, H. (2025). Numerical investigation of nonlinear interaction between salinity-and sediment-induced stratification in highly turbid estuaries and coastal seas. *Engineering Applications of Computational Fluid Mechanics*, *19*, 2443123. https://doi.org/10.1080/19942060.2024.2443123